ISSN 0869-5911, Petrology, 2010, Vol. 18, No. 4, pp. 384–415. © Pleiades Publishing, Ltd., 2010.
Original Russian Text © K.A. Savko, E.Kh. Korish, S.M. Pilyugin, T.N. Polyakova, 2010, published in Petrologiya, 2010, Vol. 18, No. 4, pp. 402–433.

Phase Relations of REE-Bearing Minerals during the Metamorphism of Carbonaceous Shales in the Tim–Yastrebovskaya Structure, Voronezh Crystalline Massif, Russia

K. A. Savko, E. Kh. Korish, S. M. Pilyugin, and T. N. Polyakova

Voronezh State University, Universitetskaya pl. 1, Voronezh, 394006 Russia

e-mail: ksavko@geol.vsu.ru

Received October 20, 2009; in final form, February 15, 2010

Abstract—Paleoproterozoic carbonaceous shales in the Tim-Yastrebovskii ancient rift, which underwent zonal metamorphism at 350–550°C, contain REE mineralization of silicates (allanite, thorite, and Ce–P huttonite) fluorcarbonates (bastnaesite and synchysite), phosphates (monazite and xenotime), and REE-bearing apatite. The reason for the wide occurrence of bastnaesite and other REE minerals is relatively high REE concentrations in the sulfide-bearing carbonaceous shales, with these elements accumulated in the organic matter in the course of diagenesis. Reaction textures with REE-bearing chlorite, bastnaesite, and allanite suggest that REE-bearing chlorite and bastnaesite provided REE for the forming of higher temperature allanite and monazite. This is corroborated by the REE patterns of the monazite, allanite, and bastnaesite, which are almost identical and are characterized by the strong predominance of LREE. The replacements of REE minerals during metamorphism at 350–550°C took place via a number successive transitions: (1) $Mnz \longrightarrow Aln$, $Chl_{REE} \longrightarrow Bst$, $Chl_{REE} \longrightarrow Aln$, $Bst \longrightarrow Aln$ and (2) $Bst \longrightarrow Mnz$ and $Ap_{LREE} \longrightarrow Mnz$. These replacements can be accounted for by prograde metamorphic reactions.

DOI: 10.1134/S0869591110040053

INTRODUCTION

A few past decades witnessed significant achievements in the reproduction of the evolution of metamorphic events via studying phase equilibria of critical minerals and the application of mineralogical thermobarometry and isotopic dating. Studies of assemblages of accessory minerals, first of all, those with REE, were launched more recently, with interest in them was stirred up largely due to progress in methods of the in-situ analysis (CHIME) and isotopic dating (SHRIMP) of metamorphic events with the use of monazite, xenotime, thorite, allanite, sphene, bastnaesite, and other minerals that can contain appreciable concentrations of Th, Pb, and U.

The forming and decomposition reactions of REE minerals during metamorphism are still understood inadequately poorly. The two viewpoints concerning this problem are as follows: (1) no rock-forming aluminosilicates, which contain practically no REE, can participate in the forming and decomposition of REE minerals, and (2) REE minerals (first of all, monazite and xenotime) are formed as byproducts of reactions involving aluminosilicates (garnet, andalusite, staurolite, chlorite, and others) and resulting in the release of REE (Spear and Pyle, 2003), whose concentrations in the aluminosilicates were on the order of a few dozen ppm.

The reactions without aluminosilicate phases documented in much detail in metapelites are the forming of allanite during the decomposition of detrital monazite under greenschist facies conditions (Smith and Barero, 1990; Wing et al., 2003), the replacement of the assemblage of florencite with synchysite by the association of allanite with synchysite at HP–LT metamorphism (Janots et al., 2006), and the high-temperature replacement of allanite by metamorphic monazite under epidote-amphibolite facies conditions (Wing et al., 2003; Janots et al., 2008; Janots et al., 2009; Tomkins and Pattison, 2007; and others). The forming of monazite duirng the partial decomposition of REE-apatite in high-pressure rocks of the Bohemian Massif was described in (Finger and Krenn, 2007), and the origin of this mineral at the sacrifice of apatite and sphene was described in cordierite–orthoamphibole gneisses in Manitouwadge, Ontario, (Pan, 1997) and Rogaland orthogneisses in Southwestern Norway (Bingen et al., 1996).

The other viewpoint implies that appreciable amounts of LREE and P can be contained in "usual" silicates, and their decomposition in the absence of high-temperature REE minerals can produce monazite (Lanzirotti and Hanson, 1996; Kohn and Malloy, 2004; Gibson et al., 2004). This conclusion is based on a dramatic increase in the monazite content with the

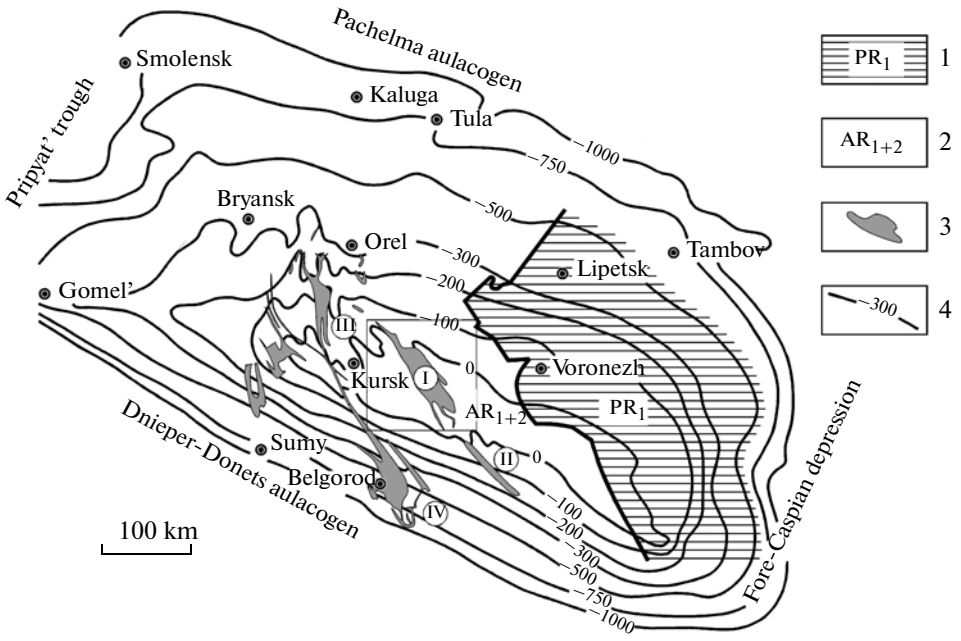

Fig. 1. Structural zones in the Precambrian basement of the Voronezh Crystalline Massif.
(1) Paleoproterozoic rocks of the Voronezh block; (2) Archean rocks of the Kursk block; (3) synclinal structures filled with Paleoproterozoic rocks: (I) Tim–Yastrebovskaya, (II) Volotovskaya, (III) Mikhailovskaya, (IV) Belgorodskaya; (4) equal depth lines for the Precambrian basement surface.

appearance of staurolite and on an increase in the LREE and P concentrations (to a few dozen ppm) in garnet, plagioclase, biotite, muscovite, and chlorite in the absence of these components in the staurolite (Kohn and Malloy, 2004). The growth of monazite and xenotime via the partial decomposition of garnet in metapelites was documented in the Canadian Cordilleras (Gibson et al., 2004) and in contact metamorphic rocks in northern Labradore (McFarlane et al., 2005).

Paleoproterozoic carbonaceous shales in the Tim–Yastrebovskaya structure in the Voronezh Crystalline Massif (VCM) were determined to contain REE mineralization of phosphates (monazite and xenotime, and REE bearing apatite), fluorcarbonates (bastnaesite and synchysite), and silicates (allanite, Ce–P huttonite, and thorite). These REE minerals sometimes show reaction relations both with one another and with chlorite, which occurs as clusters in the carbonaceous shales.

This publication is centered on the interpretation of the textural relations of REE minerals in carbonaceous shales from the Tim–Yastrebovskaya structure with the aim of reproducing the succession of reactions of the forming, growth, and decomposition of mineral phases during low- and middle-temperature zonal metamorphism.

GEOLOGY

The Tim–Yastrebovskaya structure is one of the largest Paleoproterozoic synforms at VCM: it extends for 130 km from northwest to southeast at a width of 10–30 km and a depth of 5–8 km (as inferred from geophysical data) (Fig. 1). In terms of geodynamics, the structure is an acient continental rift that started to develop in the Paleoproterozoic on a Neoarchean protoplatform.

The Tim–Yastrebovskaya structure and the structures surrounding it are made up of Archean and Paleoproterozoic rocks (Fig. 2). Archean rocks in structures around the Tim–Yastrebovskaya structure compose thick sequences of high-grade metamorphosed sedimentary and volcanic–sedimentary rocks of the Oboyan Complex and Mikhailovskaya Group. The Tim–Yastrebovskaya structure itself is filled with Paleoproterozoic rocks of the Kursk and overlying Oskol groups.

Rocks of the Kursk Group compose the southwestern flank of the structure and its northwestern and southeastern closures and are dominated by metapelites and metapsammites of the Stoilenskaya Formation and thick sequences of magnetite quartzites with beds of schists of the Korobkovskaya Formation (approximately 1000 m in thickness and more). The exact age of BIF in the Kursk Group is uncertain. The lower age boundary was constrained to the Neoarchean using the underlying potassic rhyolite of the Lebedinskaya Formation: U–Pb zircon age of

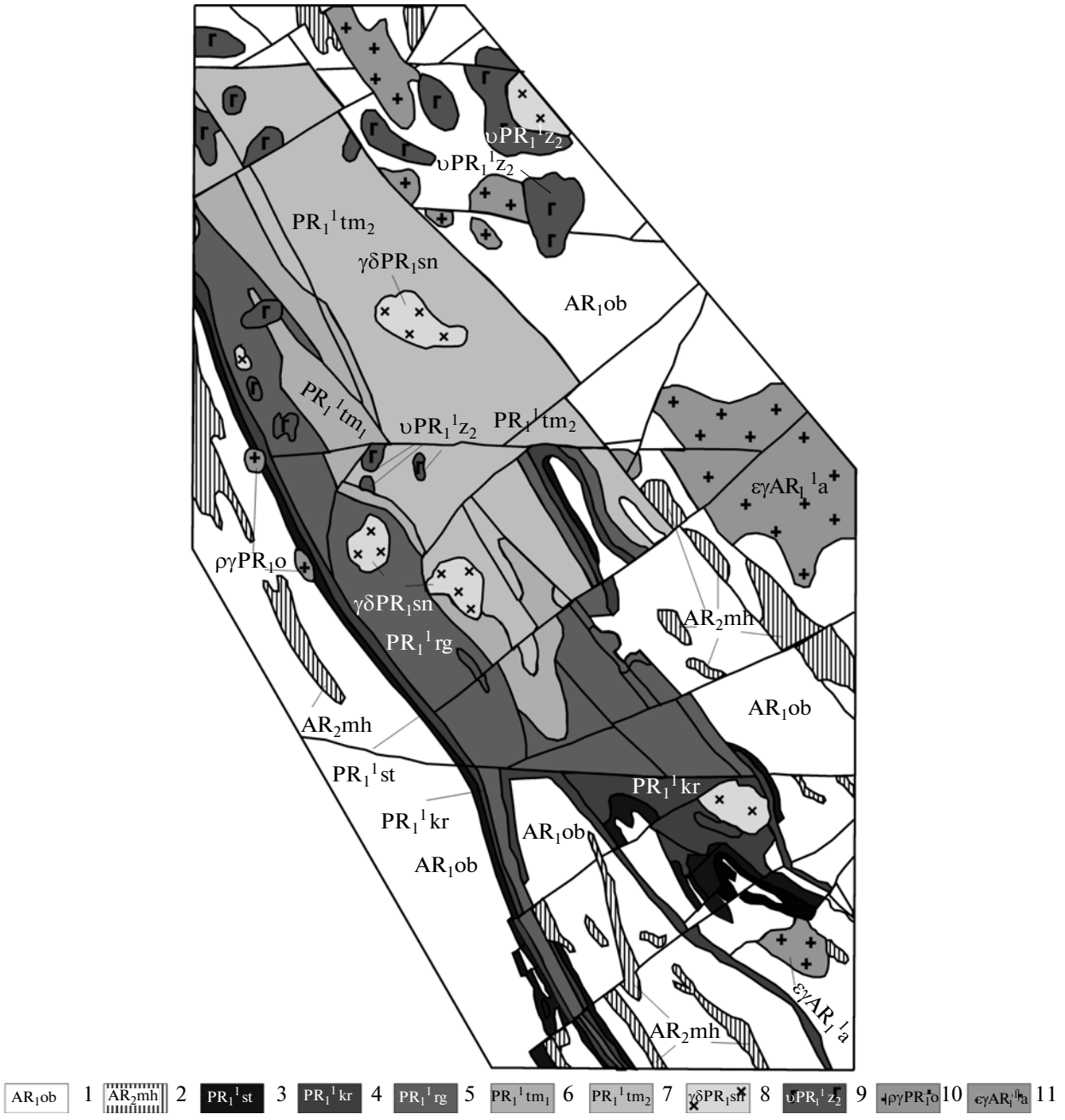

Fig. 2. Schematic geological map of the Tim–Yastrebovskaya structure.

(1) Oboyan Complex (gneisses, granite-gneisses, migmatites, granulites, and magmas); (2) Mikhailovskaya Group (two-mica and chlorite schists; amphibolites, komatiites, rhyolites, and dacites); (3–4) Kursk Group: (3) Stoilenskaya Formation (metasandstones, quartzites, phyllite-like shales, and mica schists), (4) Korobkovskaya Formation (BIF, phyllite-like shales, and mica schists); (5–7) Oskol Group: (5) Rogovskaya Formation (quartz–biotite and quartz–sericite schists, dolomites, marbles); (6–7) Timskaya Formation: (6) lower subformation (quartz-biotite carbonaceous shales, calc-silicate rocks, and metamorphosed mafic and acid volcanic rocks), (7) upper subformation (carbonaceous shales and metamorphosed mafic and acid volcanic rocks); (8–11) intrusive complexes: (8) Stoilo-Nikolaevskii, (9) Zolotukhinskii, (10) Oskol, (11) Atamanskii.

2590 ± 44 Ma (Shcherbak et al., 1992. Its upper age boundary can be estimated based on the age of the overlying acid volcanics in the Mikhailovskaya synform: close to 2170 Ma (Artemenko, 1998).

The composition and age of the Oskol Group are determined by cyclically alternating conglomerates, gritstones, and metasandstones, which grade into carbonate–mica schists with beds of amphibolites, metamorphosed dolomites, and limestones and widespread carbon-bearing rocks and volcanics in the upper part of the sequence. The thickness of the Oskol Group was estimated at a few kilometers. The group is subdivided

into the older terrigenous–carbonate Rogovskaya Formation and the younger Timskaya Formation, which is dominated by terrigenous–volcanic rocks. The Rogovskay Formation occurs along the southwestern slope of the Tim–Yastrebovskaya structure and in its northeastern closure and consists of variably marmorized limestone, which is enriched in carbonaceous matter in single beds. The Timskaya Formation is predominant in the Tim–Yastrebovskaya structure (Fig. 2) and is classified into a lower and an upper subformation.

The Lower Timskaya Subformation has a pronounced cyclic structure with widespread sulfide–carbonaceous schists and subordinate beds of metasandstones, quartzites, and calc-silicate rocks.

The Upper Timskaya Subformation is dominated by volcanic rocks. The lower portion of its vertical section is composed of carbonaceous and carbon-free mica schists, and its upper part consists mostly of metavolcanics with sandstone and schist beds. No precise dates have ever been obtained for rocks of the Oskol Group.

The collision of Sarmatia and Volgouralia at approximately 2.1 Ga resulted in the closure of the Kursk block. Crustal melting zones developed there in an compressional environment, and a number of intrusive complexes was formed in various parts of the collision structure (Kholin, 2001). In the closure structures of the Kursk block, these are the Stoilovo-Nikolaevskii granitoid complex (2085 ± 5 Ma), Shchebekinskii syenite complex (2066 ± 14 Ma), and Malinovskii granite complex (2040 ± 30 Ma) (Artemenko, 1998). The same evolutionary phase was marked by the origin of the andesite unit in the Glazunovskaya Formation at 2151 ± 79 Ma (Artemenko, 1998).

METAMORPHISM

The zonal metamorphism of rocks of the Tim–Yastrebovskaya structure was studied in much detail (Savko and Polyakova, 2001; Polyakova et al., 2005, 2006) at an extent permitted by the poorly exposed study area with a thin network of boreholes. When the metamorphic zones of the metapelites were mapped, the following zones and subzones were recognized: the biotite zone with chlorite–potassic feldspar and biotite–muscovite subzones and the garnet and staurolite zones with staurolite–chlorite andalusite–biotite, and cordierite–biotite subzones (Fig. 3).

Biotite zone. *Chlorite–potassic feldspar subzone.* The lowest temperature mineral assemblages in the examined metapelites of the Tim–Yastrebovskaya structure are *Chl* + *Kfs* + *Bt* and *Chl* + *Kfs* + *Ms* rocks (Fig. 4a). The stability of the *Chl* + *Kfs* association constrain the lowest temperature metamorphic conditions to the lower part of the biotite subfacies of the greenschist facies (chlorite–potassic feldspar subzone). The stability of the *Chl* + *Kfs* association is comparable with that of the *Bt* + *Ms* association in the metapelite intercalations (Fig. 4b). This association can be generated in this subzone only in rocks that originally contained muscovite, stilpnomelane, and potassic feldspar, with biotite produced there by the reaction $St + Kfs = Bt + Qtz + H_2O$. Hence, the lowest temperature metamorphic conditions in the Tim–Yastrebovskaya structure are constrained, on the one hand, by the decomposition of the assemblage of stilpnomelane with potassic feldspar with the origin of biotite and, on the other hand, by the stability of the chlorite plus potassic feldspar association, which characterizes the upper part of the chlorite–potassic feldspar subzone of the biotite zone.

Biotite–muscovite subzone. In the higher grade metamorphic rocks, the association of chlorite with potassic feldspar gives way to the association of biotite with muscovite ($Chl + Kfs = Bt + Ms + Qtz + H_2O$) (Fig. 4b). Consequently, the metapelites bear mineral assemblages with either excess potassic feldspar (*Bt* + *Kfs* + *Ms*) or chlorite (*Bt* + *Chl* + *Ms*) stable in the upper part of the biotite zone, which we refer to as the biotite–muscovite subzone.

The metapelites with excess potassic feldspar sometimes contain garnet rich in spessartine ($Sps_{75-80}Grs_{13-14}Prp_{4-6}Alm_{1-5}$) (Fig. 4c), whose occurrence in the biotite zone, even in the pre-biotite subfacies, is not unusual. Spessartine is formed in the biotite or pre-biotite subfacies not by a reaction of chlorite with quartz but by the decomposition of Mn-bearing carbonates.

Garnet zone. Starting in the upper greenschist metamorphic facies, garnet is formed by the reaction $Chl + Qtz = Grt + H_2O$. The appearance of garnet results in the *Bt* + *Grt*, *Chl* + *Grt*, *Bt* + *Chl* + *Grt*, *Bt* + *Grt* + *Ms*, and *Bt* + *Chl* + *Grt* + *Ms* assemblages in low-Al metapelites of the Tim–Yastrebovskaya structure and the *Grt* + *Ms* and *Chl* + *Grt* + *Ms* assemblage in more aluminous metapelites (Figs. 4d, 4e). Highly magnesian chlorite remains stable up to the high-temperature region of the staurolite facies in the *Bt* + *Chl* + *Ms* and *Chl* + *Ms* associations.

Staurolite zone. *Staurolite–chlorite subzone.* Further changes in the metamorphic conditions are marked by the appearance of staurolite in the metapelites. The Tim–Yastrebovskaya structure contains no metapelites with the *And* + *Chl* + *Cld* assemblage, and staurolite is formed in the metapelites by the reaction $Ms + Grt + Chl \longrightarrow St + Bt + Qtz + H_2O$, which testifies to metamorphic conditions of the staurolite–muscovite subfacies (Figs. 5a, 5b) (Korikovsky, 1979).

After staurolite crystallization, metapelites of the Tim–Yastrebovskaya structure contain the assemblages *Bt* + *Grt* + *Ms* + *St*, *Bt* + *Grt* + *St*, *Bt* + *Ms* + *St*, and *Bt* + *Chl* + *Grt* + *St* (Figs. 5a, 5b). The assemblages *Bt* + *Grt*, *Chl* + *Grt*, *Bt* + *Chl* + *Grt*, and *Bt* + *Grt* + *Ms* formed during earlier metamorphic stages remain stable throughout the whole temperature range of the

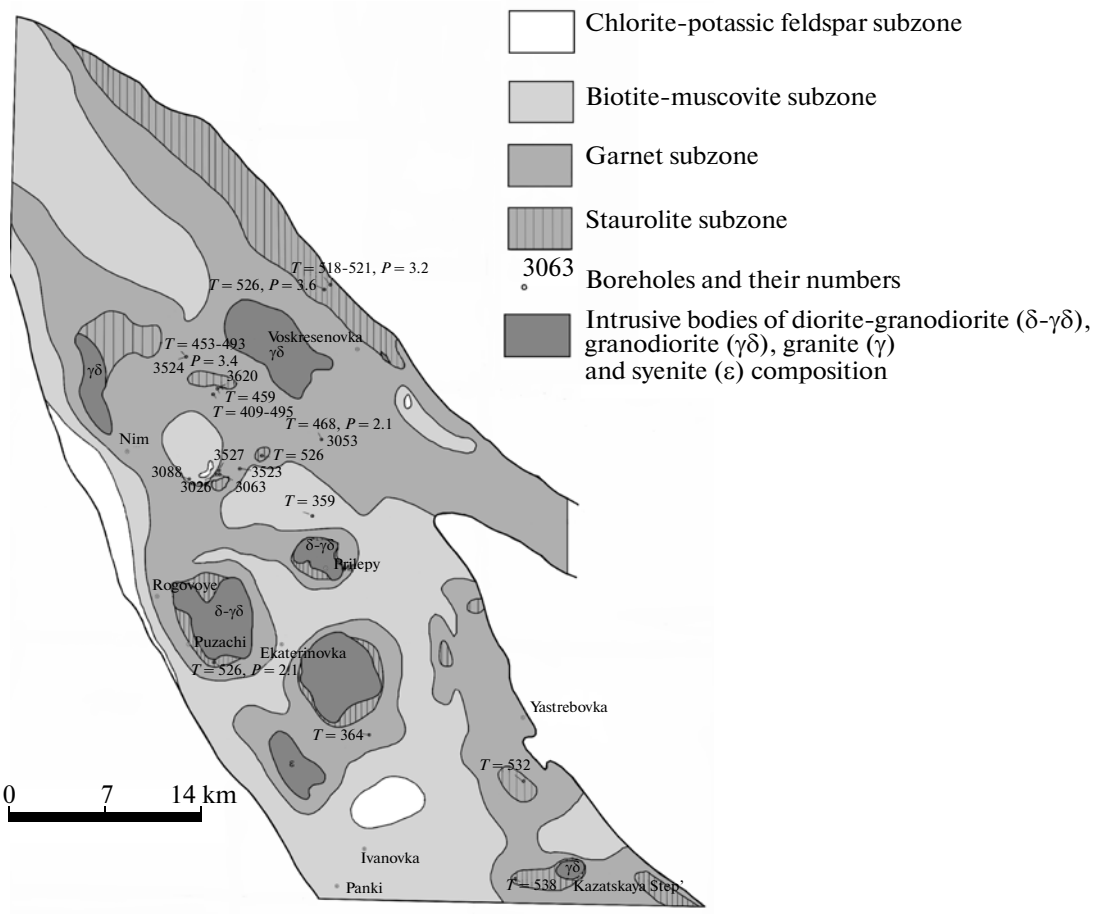

Fig. 3. Map showing the metamorphic zoning of the Tim–Yastrebovskaya structure.

staurolite–chlorite subzone. An increase in the metamorphic grade results solely in changes in the composition of minerals due to the redistribution of components between coexisting minerals.

Andalusite–biotite subzone. Samples from some boreholes drilled through metapelites of the staurolite facies contain mineral assemblages with andalusite. In the low-temperature portion of the staurolite zone, andalusite was formed by the reaction $St + Chl + Ms = And + Bt + Qtz$, which corresponds to the lower boundary of the andalusite (kyanite, sillimanite)–biotite–staurolite subfacies according to (Korikovsky, 1979).

Metapelites of the andalusite–biotite subzone of the Tim–Yastrebovskaya structure contain the *And* + *Bt* + *Ms* and *And* + *Bt* + *Ms* + *St* (Figs. 5c, 5d) assemblages and many mineral associations of the staurolite–chlorite–muscovite subfacies that are still stable.

Cordierite–biotite subzone. The highest temperature mineral assemblage of our metapelites is *Bt* + *Crd* (Fig. 5e). Cordierite first crystallizes in the upper part of the greenschist facies in aluminous rocks, according to the reaction $Chl + And + Qtz = Crd + H_2O$ (Korikovsky, 1979). However, the association of cordierite with biotite appears in the upper part of the andalusite–biotite subfacies of the staurolite facies, which is referred to as the cordierite–biotite subzone. This grade can be recognized only in metapelites with highly magnesian chlorite, which ensures the stability of such mineral assemblages as *Bt* + *Chl* + *Ms* and *Chl* + *Ms* up to the upper part of the staurolite facies. In the cordierite–biotite zone, magnesian chlorite gives way to the *Bt* + *Crd* assemblage, which is produced by the reaction $Chl + Ms + Qtz = Bt + Crd + H_2O$ (Fig. 5e).

The metamorphic *P-T* conditions determined for the biotite zone by mineralogical thermobarometry are <350–400°C for the low-temperature chlorite–potassic feldspar subzone, 400–500°C for the garnet zone, and 500–560°C for the staurolite zone at pressures of 2.1–3.6 kbar (Polyakova et al., 2006). The distribution of the metamorphic zones shows a striped and patchy mosaic pattern: the lowest grade rocks of the greenschist facies are prone to be restricted to the southwestern flank of the structure, in which a narrow meridionally elongated fragment of the chlorite–potassic feldspar subzone was mapped. Higher grade rocks (garnet zone) are restricted to the northeastern flank of the structure. The central part of the Tim–

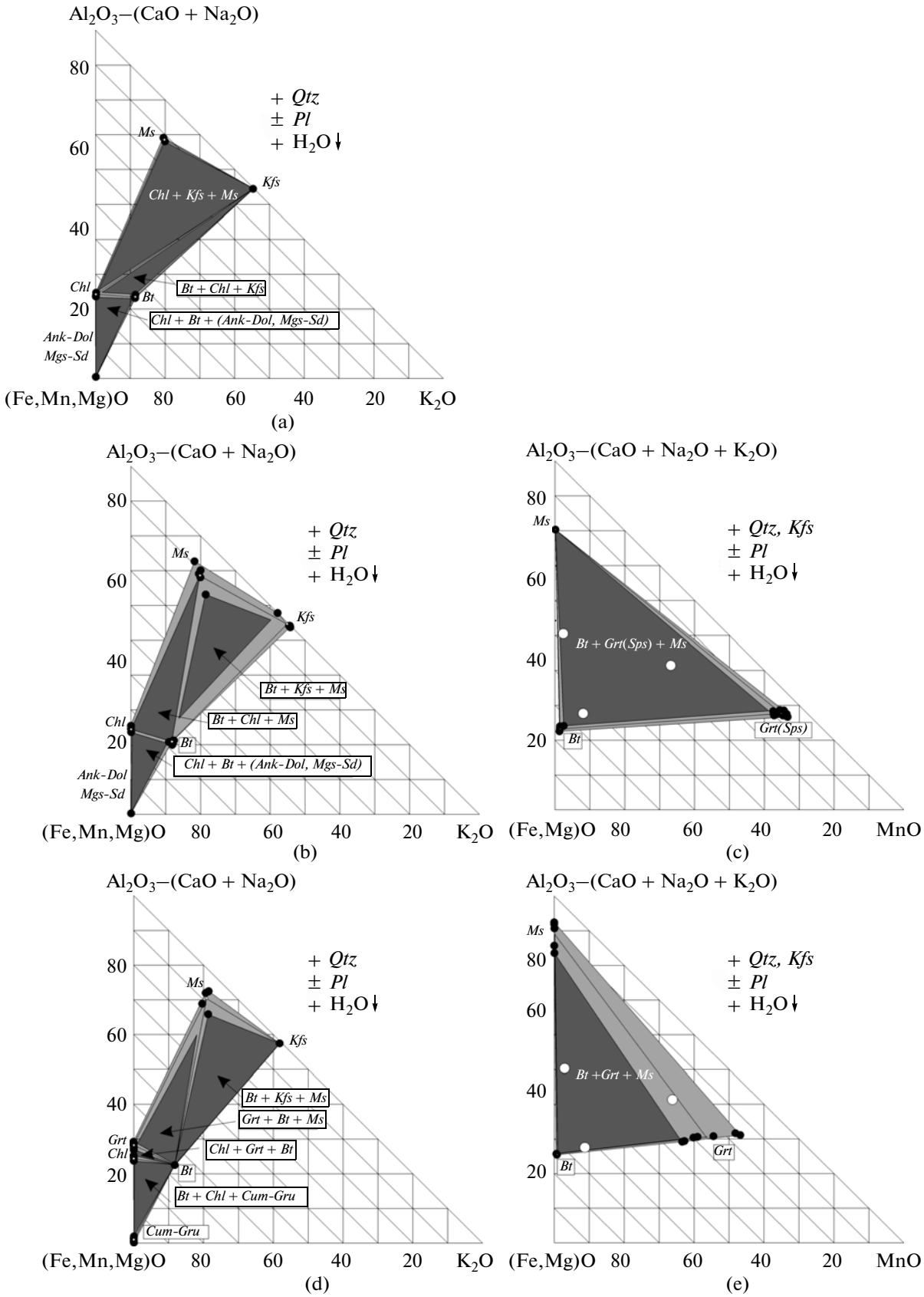

Fig. 4. Greenschist-facies phase equilibria in metapelites from the Tim–Yastrebovskaya structure.
(a–c) Biotite zone: (a) chlorite-potassic feldspar subzone, (b, c) biotite-muscovite subzone, (d, e) garnet subzone, (c, e) in K_2O-rich MnO-rich metapelites. Open circles show the composition of Mn-rich metapelites.

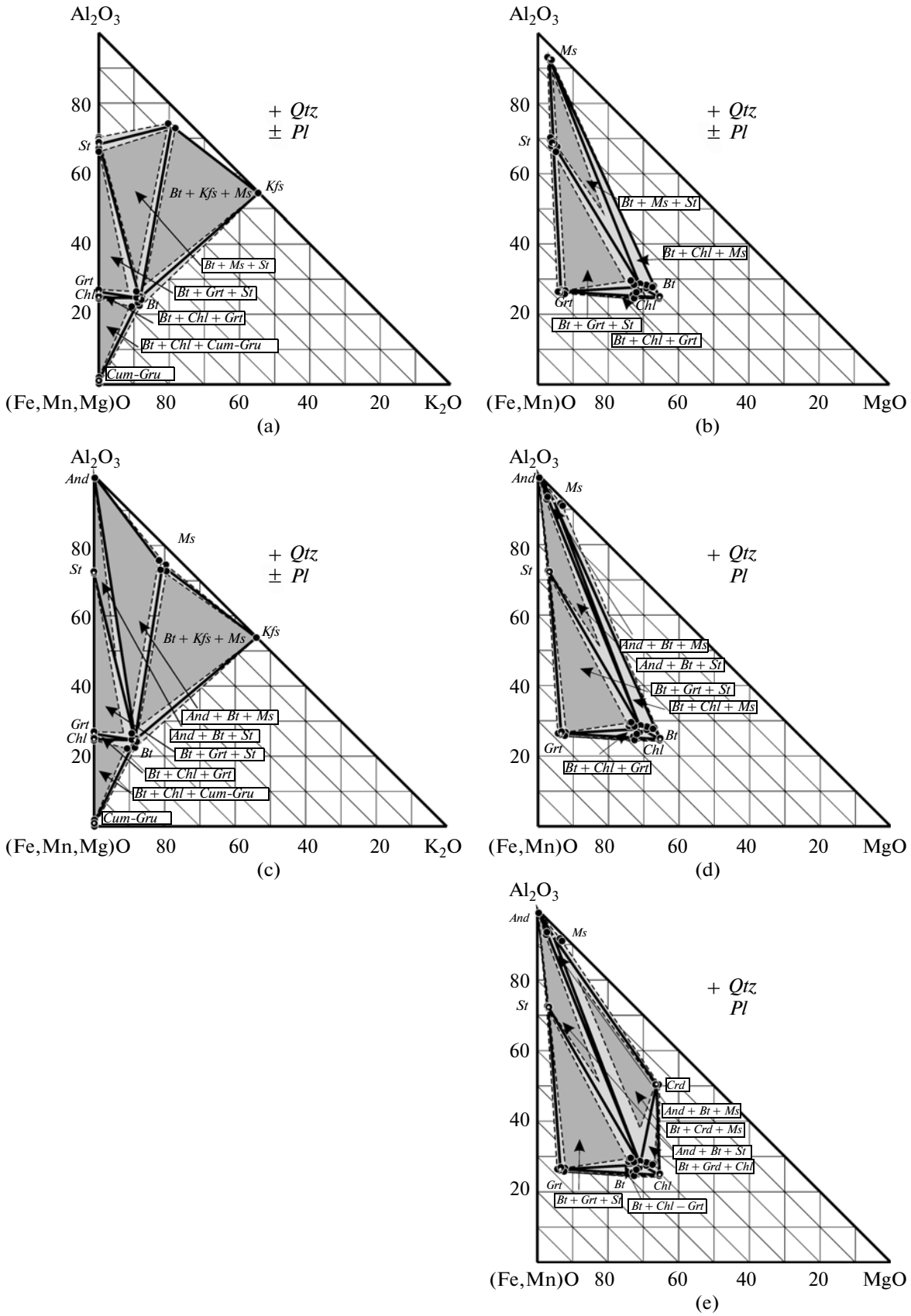

Fig. 5. Staurolite-facies phase equilibria in metapelites from the Tim–Yastrebovskaya structure.
(a, b) Staurolite-chlorite-muscovite subfacies, (c, d) andalusite-biotite subfacies; (e) cordierite-biotite subfacies.

Yastrebovskaya structure shows a complicated patchy mosaic distribution of lower and higher temperature metamorphic zones, with concentrically zoned thermal aureoles around intrusions of the Stoilo–Nikolaevskii Complex (Fig. 3).

The low-temperature metamorphic zones exhibit obvious evidence that minerals and mineral aggregates grew synchronously with folding. In contact aureoles around intrusions of the Stoilo–Nikolaevskii Complex, randomly oriented mineral crystals overprint the earlier schistosity.

The metamorphic complex was formed by two successive metamorphic events. The earlier one affected the whole complex of Paleoproterozoic rocks in the Tim–Yastrebovskaya structure and was manifested regionally. These processes were synchronous with folding and ductile deformations, as the temperature grew from 350 to 560°C at a pressure increase to 3.6 kbar. The heat flux thereby increased from the southwestern to northeastern flank of the structure (Fig. 3). The geothermal gradient of the regional metamorphism was 40–50°C/km. The other, later metamorphic even was manifested locally, in the contact aureoles of intrusions of the Stoilo–Nikolaevskii Complex. The temperature gradient increased to 70–80°C/km at a pressure decrease to 2.1 kbar.

METHODS

All of our samples were obtained from borehole core, which was thorough described in the field. Trace and minor elements were analyzed by inductively coupled plasma with mass spectrometry (ICP-MS) at the Certified Test Analytical Center of the Institute of Microelectronic Technology and Ultrahigh-Purity Materials, Russian Academy of Sciences (ASITs IPTM RAS). Rock samples were decomposed by acids in a closed system. The chemical yield during decomposition was controlled with the use of ^{161}Dy. According to these data, the samples were 100–64% decomposed, perhaps, due to carbonaceous matter that was not decomposed, as can be seen from the presence of variable amounts of black residual material of the samples after their decomposition. The detection limits were 0.02–0.03 ppm for REE, Hf, Ta, Th, and U; 0.03–0.05 ppm for Nb, Be, and Co; 0.1 ppm for Li, Ni, Ga, and Y; 0.2 ppm for Zr; 0.3 ppm for Rb, Sr, and Ba; and 1–2 ppm for Cu, Zn, V, and Cr. The accuracy of the analyses was controlled by replicate analyses of the SSL-1 (GSO 3191-85) certified Russian standard of metamorphic schist. The relative standard deviation was no greater than 0.3 for all elements at concentrations of the elements no higher than 5 detection limits and no higher than 0.15 at >5 detection limits.

Borehole core material was utilized to prepare polished thin sections, which were first examined under an optical microscope and then on an Jeol 6380 LV electron microscope equipped with an INCA 250 EDS analyzer at the Voronezh State University and on a TESCAN VEGA II XMU electron microscope with an INCA X-SIGHT EDS analyzer at the Institute of Experimental Mineralogy, Russian Academy of Sciences. REE minerals were identified under an optical microscope and in BSE images; their qualitative analyses were carried out with the use of standard REE samples (Table 1).

Analytical conditions at Jeol 6380 LV (Voronezh State University) were as follows: the accelerating voltage was 20 kV, the electron absorption current at Cu was 1–2 nA, the beam diameter was 200 nm, and the focal length was 10 mm. The accelerating voltage at the TESCAN VEGA II XMU SEM was 20 kV, the focal length was 25 mm, the electron absorption current on Co was 0.3 nA, and the beam diameter was 260 nm.

PETROGRAPHY AND PETROCHEMISTRY OF CARBONACEOUS SHALES

The metasedimentary rocks of the Timskaya Formation are gray, dark gray, or black, often greenish thin- or fine-grained. In terms of grain size and proportions of chlorite, micas, and quartz–feldspar aggregates, they show gradual transitions from metamorphosed silt–pelite to psammite. The rocks typically have a metapsammites textures, defined by the presence of clastic quartz grains of variable roundness. The texture of the shales and their groundmass of the metapsammites is lepido-granoblastic. If large (up to 2–3 mm) grains of metamorphic minerals appear in the rocks, the texture of the rocks becomes porphyroblastic.

Carbonaceous mica–quartz shales are the most widely spread rock type of the Timskaya Formation. The major rock-forming minerals are (in addition to quartz) muscovite, biotite, chlorite, and pyrite, and the rocks may contain minor calcite concentrations.

The micas usually occur as small (a few hundredths of a millimeter) flakes with abundant dust of carbonaceous matter, which makes the minerals practically opaque.

Chlorite is widespread in the carbonaceous shales as relatively large (up to 0.3 mm) laths and their accumulations (clusters) and as small (0.05 mm) flakes of greenish brown color. The low-temperature chlorite shows variations in their $X_{Fe} = 0.53–0.89\%$.

The highly carbonaceous shales are rich in sulfides, whose contents are correlated with the content of carbonaceous matter. Sulfide form thin-grained dissemination in the carbonaceous matter, pockets of fine-grained pyrrhotite and pyrite (up to a few centimeters across), and large crystals in rocks. The total contents of sulfides may be as high as 30%.

Carbonaceous matter occurs as fine dust, lenses, lenticular accumulations, and practically monomineralic aggregates of graphite.

Table 1. Standards used in the quantitative analysis of the REE-bearing minerals

Element	Standard	
	Jeol 6380 scanning electron microscope equipped with an INCA 250 energy-dispersive analyzer (Voronezh State University)	TESCAN VEGA II xmu scanning electron microscope equipped with an INCA x-sight energy-dispersive analyzer (Institute of Experimental Mineralogy, Russian Academy of Sciences)
Y	Y	YPO_4
La	LaB_6	$LaPO_4$
Ce	CeO_2	$CePO_4$
Pr	PrF_3	$PrPO_4$
Nd	NdF_3	$NdPO_4$
Sm	SmF_3	$SmPO_4$
Eu	EuF_3	$EuPO_4$
Gd	GdF_3	$GdPO_4$
Tb	TbF_3	$TbPO_4$
Dy	DyF_3	$DyPO_4$
Ho	HoF_3	$HoPO_4$
Er	ErF_3	$ErPO_4$
Tm	TmF_3	$TmPO_4$
Yb	YbF_3	$YbPO_4$
Lu	LuF_3	$LuPO_4$
Th	ThO_2	ThO_2
U	UO_2	UO_2

The carbonaceous shales contain beds with elevated MnO contents (4–9 wt %), ranging from 2 to 10 m in thickness. These rocks contain Mn-rich minerals: spessartine, Mn-calcite, and Mn sulfide alabandite.

The REE mineralization is constrained mostly to highly carbonaceous varieties of the shales that contain >10% carbonaceous matter. The highly carbonaceous shales of the Timskaya Formation can be subdivided into the following types according to their mineral composition: garnet–quartz–biotite, two mica, quartz–biotite, quartz–muscovite, quartz–graphite, and chlorite–biotite–muscovite shales. All of these varieties of the carbonaceous shales intercalate in the vertical section of the formation with low-carbonaceous and carbon-free quartz–biotite and two-mica shales and with dolomite, quartzite, and quartzite-sandstone beds. Carbonaceous shales of the Timskaya Formation have a variable mineralogical composition and, consequently, variable petrochemistry. However, all of them are rich in organic carbon (C_{org} > 10%), sulfur, phosphorus, and iron, with FeO strongly dominating over Fe_2O_3 (Table 2).

The quartz–muscovite carbonaceous shales are characterized by the predominance of FeO over Fe_2O_3, at a total Fe content close to the clarke, and by the predominance of K_2O over Na_2O (Table 2); the rocks typically bear elevated concentrations of sulfur and C_{org} and low contents of carbonates.

The quartz–muscovite carbonaceous shales typically contain elevated concentrations of a broad spectrum of minor and trace elements (Table 3). The total REE concentrations vary from 146 to 777 ppm, which is higher than the usual concentrations in metapelites. Significant variations from sample to sample are shown by the total concentrations of LREE: from 64 to 528 ppm. The chondrite-normalized REE patterns (Fig. 6) show negative Eu anomalies (Eu/Eu* = 0.40–0.67) and significant negative slopes ($(La/Yb)_n$ = 2.7–29.9, $(Gd/Yb)_n$ = 0.71–3.61, and $(LREE/HREE)_n$ = 1.09–8.39; Table 3). These features are typical of post-Archean clay shales formed from detrital material with erosion products of granitoid rocks (Likhanov et al., 2008). The Ce/Ce* ratio of the carbonaceous shales varies within a narrow range of 0.98–1.21, which suggests, particularly considered together with $(LREE/HREE)_n$ = 1.09–8.39, that sedimentation took place at shallow water depths on the shelf, in a humid climate, and in a tectonically quiet setting (Balashov, 1976; Murrey et al., 1990).

REE minerals are spread particularly widely in the quartz–muscovite carbonaceous shales. The REE minerals are allanite, bastnaesite, synchysite, monazite, xenotime, and thorite. Other accessory minerals are ilmenite, rutile, ilmenorutile (with 4.1–5.9 wt % Nb_2O_3 and 0.6–1.0 wt % Ta_2O_5), magnetite, sphene, chalcopyrite, sphalerite, galena, arsenopyrite, cobal-

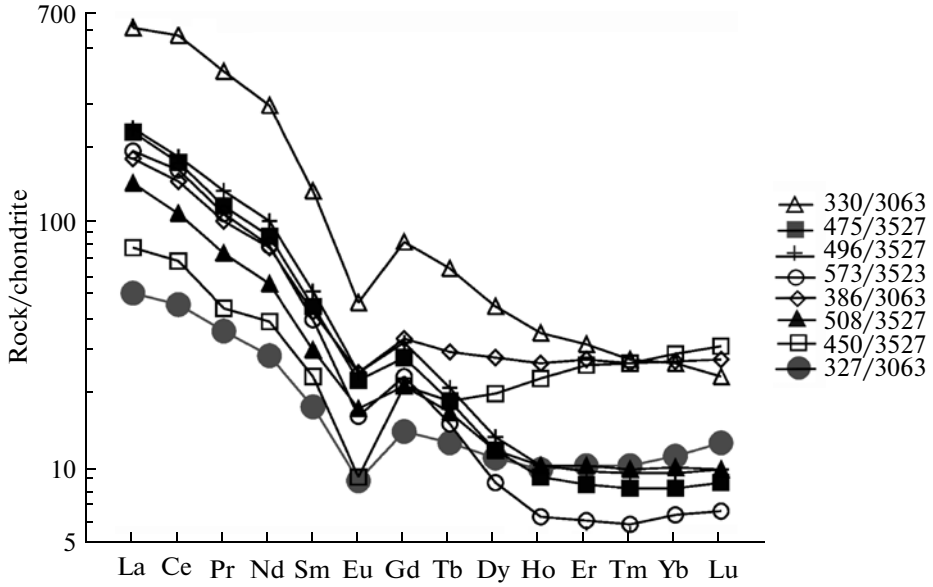

Fig. 6. Chondrite-normalized REE patterns of carbonaceous shales from the Tim–Yastrebovskaya structure.

tite, gersdorffite, alabandite, and Nb-aeschynite $(Y,Ca,Ce,Nd,Th)(Nb,Ti,Ta)_2(O,OH)$.

MINERALOGY OF THE REE-BEARING MINERALS

Allanite $[Ca,REE,Al_2(Mg,Mn,Fe)(Si_3O_{11})O(OH)]$ is an REE-bearing silicate of the epidote group. It occurs in the rocks as two morphological varieties: (1) relatively large (up to 500 μm long) prismatic crystals (porphyroblasts) with a well pronounced cleavage, submerged in a matrix, in close association with sulfide and bastnaesite inclusions (Figs. 7a, 7b, 7e, 7f); and (2) small elongated grains up to 50 μm (usually 5–20 μm) long, restricted to chlorite clusters (Figs. 7c, 7d, 8a, 8b, 8d, 8f). In addition to chlorite, allanite (2) occurs in close association with bastnaesite, pyrite, rutile (Figs. 8b, 8d), and, more rarely, monazite (Figs. 8a, 8e, 8f). Large tabular allanite (1) crystals display a zonal distribution of Fe, whose concentration decreases from the cores to rims of the grains (Table 4). Allanite (1) is richer in Fe and REE than allanite (2). It is worth mentioning that, similar to analogous rocks elsewhere (see, for example, Janots et al., 2008), our rocks contain no zonal allanite crystals with gradations from allanite to clinozoisite.

REE in the allanite are dominated by Ce (8.4–11.4 wt % Ce_2O_3), whose concentrations are almost twice as high as that of La (3.6–6.4 La_2O_3) (Table 4). In addition to these elements, the mineral contains appreciable concentrations of Nd (1.8–4.0 wt % Nd_2O_3) and bears excess Al and Ca. The Ca excess suggests that REE^{3+} are partly substituted for Ca^{2+}, and excess Al is, correspondingly, explained by the partial substitution of Fe^{2+} for Al^{3+} in the allanite structure. The Al_2O_3, CaO, and REE concentrations in our allanite samples are close to those in allanite from metapelites in other metamorphic regions (Fig. 9a).

Allanite in carbonaceous shales in the Tim–Yastrebovskaya structure is rich in Mn (3.50–6.35 wt % MnO), whose concentration is higher than that of Fe (Table 4, Fig. 9b). Allanite in metapelites from elsewhere contains practically no Mn (Fig. 9b), and, in contrast to this mineral from elsewhere, allanite in our carbonaceous shales contains 0.21–0.50 f.u. of Mn. This element can partly occupy the structural sites of Al (up to 0.5 f.u.), together with Ca, and part of M3 sites (up to 0.28 f.u.), together with Fe and Mg (Table 5), which indicates that the mineral cannot be classed with REE–Mn subgroups (for example, androsite, khristovite, Mn-dissakisite, and others) (Armbruster et al., 2006). Nevertheless, the mineral can be referred to as Mn-allanite. The reason for elevated Mn concentration in the allanite is the composition of the carbonaceous shales, which may contain up to 4–9 wt % MnO, with the corresponding metamorphic rocks Lcontaining other Mn minerals, such as spessartine, Mn-bearing calcite, and alabandite.

The fact that concentrations of $(Fe^{2+} + Mg + Mn^{2+})$ are correlated with those of (Ce + La + Nd) suggests heterovalent isomorphism $Ca^{2+} + Al^{3+} \longrightarrow REE^{3+} + (Fe^{2+}, Mn^{2+}, Mg)$. The total for the cation charge is 24.8–25, i.e., is a little bit low, perhaps, due to the partial substitution of O for OH, as is typical of allanite.

Chlorite, with inclusions of carbonaceous matter is enriched in REE and contains these elements in concentrations that can be reliably analyzed on a microprobe. REE are dominated by Ce, whose concentra-

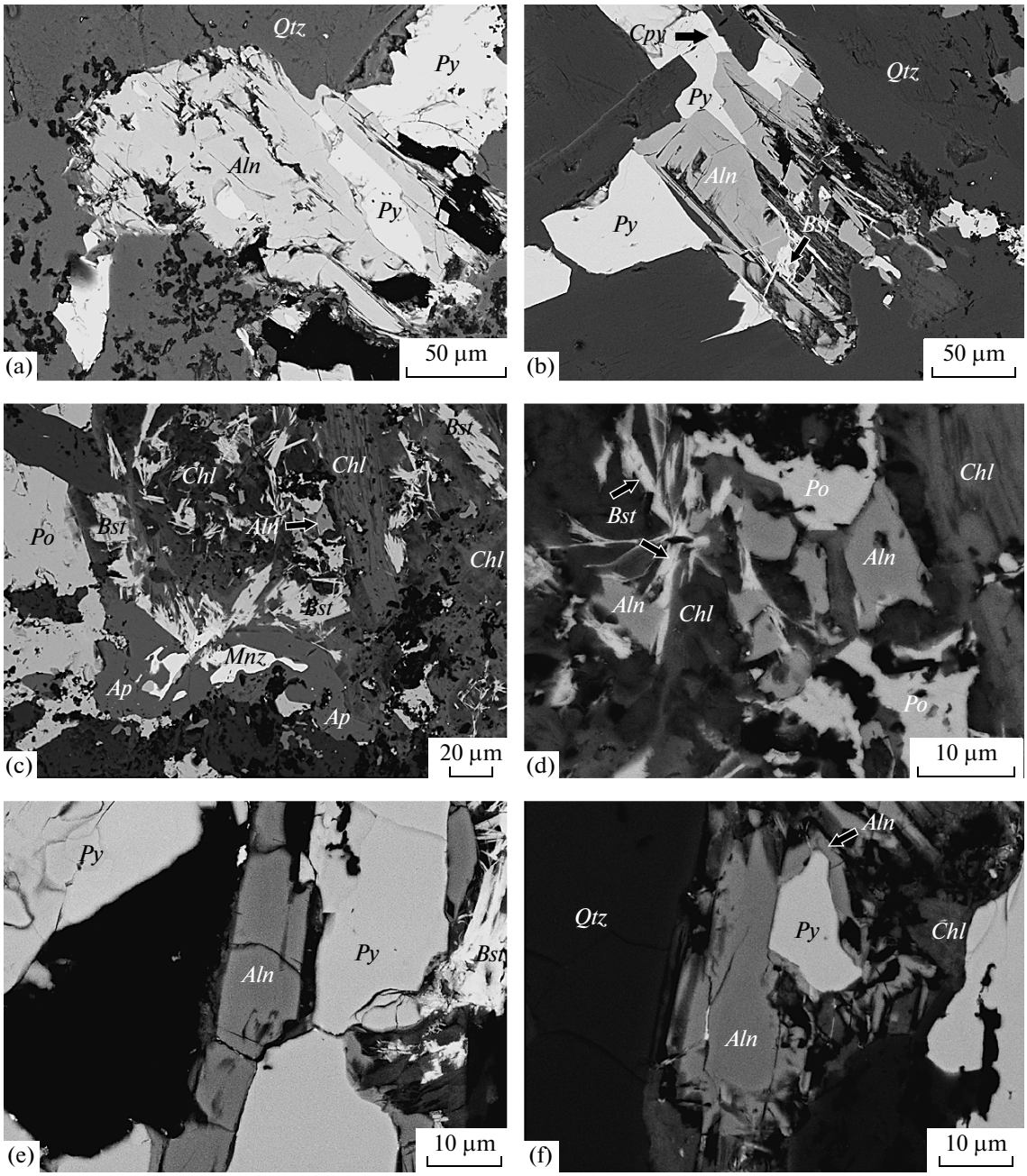

Fig. 7. Allanite relations in carbonaceous shales from the Tim–Yastrebovskaya structure.
(a, b) Large allanite crystals in association with pyrite in the rock matrix (sample 3527/472); (c, d) small allanite grains in chlorite clusters in association with bastnaesite, monazite, apatite, and pyrrhotite (sample 3620/299.5); (e, f) allanite rims around pyrite (sample 3527/496).

tions vary from 0.44 to almost 2 wt %; other REE occurring in appreciable amounts are La and Nd. The total REE concentration may come as high as 2.4 wt % (Table 6), and a single analytical spot analysis yielded 0.73 wt % Th. Figures 10a and 10b show images of REE-bearing chlorite with a bastnaesite rim replacing it and with small allanite inclusions. The core of the grain contains a large inclusion of carbonaceous matter. REE are unevenly distributed over the grain, with their highest concentrations constrained to the vicinity of the graphite inclusion and the lowest ones occurring in zones adjacent to allanite inclusions and bastnaesite rims.

Similar to allanite, **monazite** [$(LREE)PO_4$] is contained in the carbonaceous shales as two morphological types. Monazite (1) is small, no larger that 30 μm, anhedral grains in apatite (Figs. 11d, 11f) and occasional "emulsion" dissemination in large apatite crys-

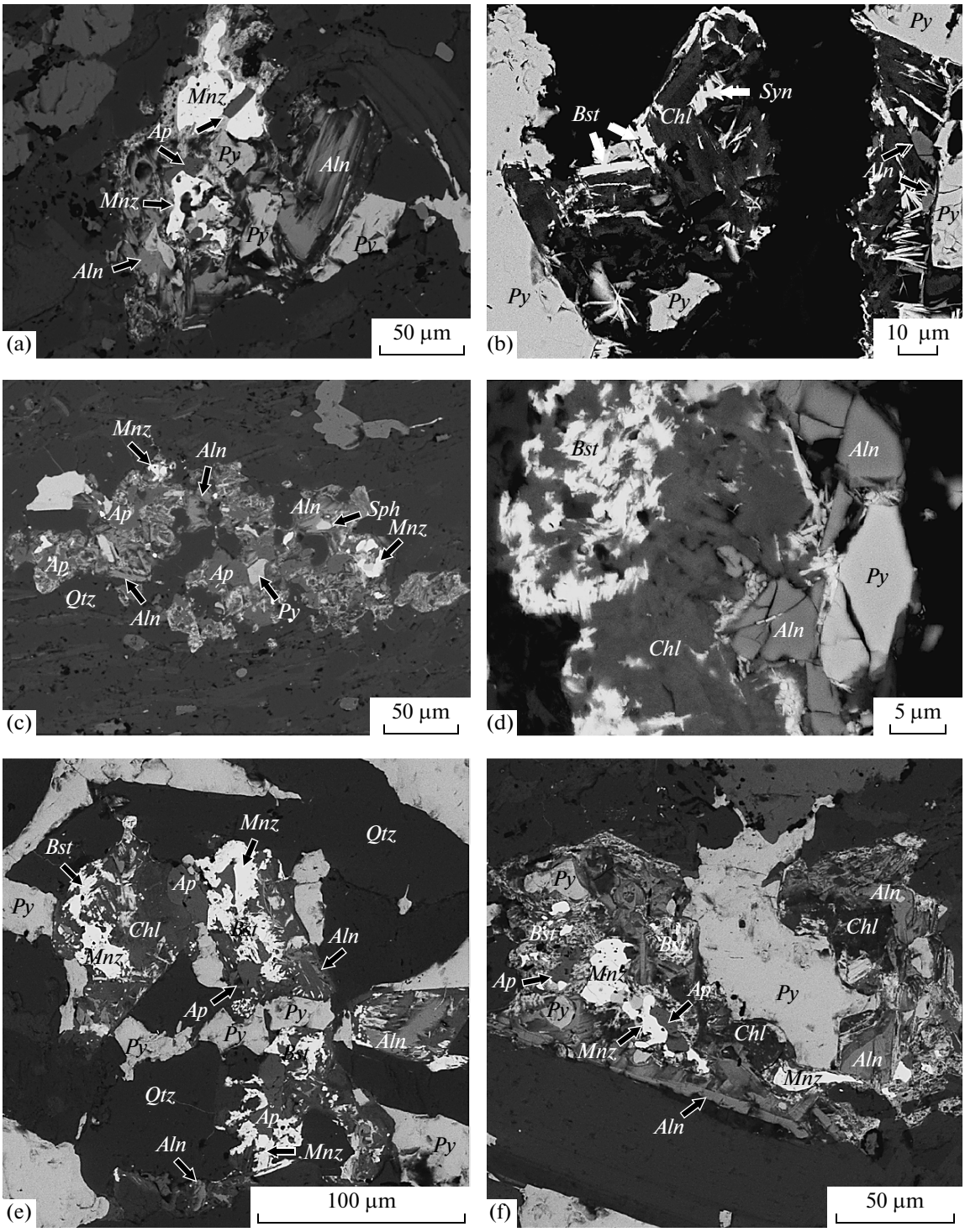

Fig. 8. REE minerals in carbonaceous shales from the Tim–Yastrebovskaya structure.

(a) Relations of allanite, monazite, and apatite in a chlorite cluster (sample 3523/511); (b) allanite in association with bastnaesite, chlorite, and pyrite (sample 3527/496); (c) association of allanite, monazite, and apatite in the matrix (sample 3523/511); (d) bastnaesite in chlorite and allanite in close association with pyrite and chlorite (sample 3527/496); (e) bastnaesite, monazite, allanite, and apatite in a chlorite cluster (sample 3523/511); (f) monazite and allanite in physical contact, the rock also contains apatite and bastnaesite (sample 3523/511).

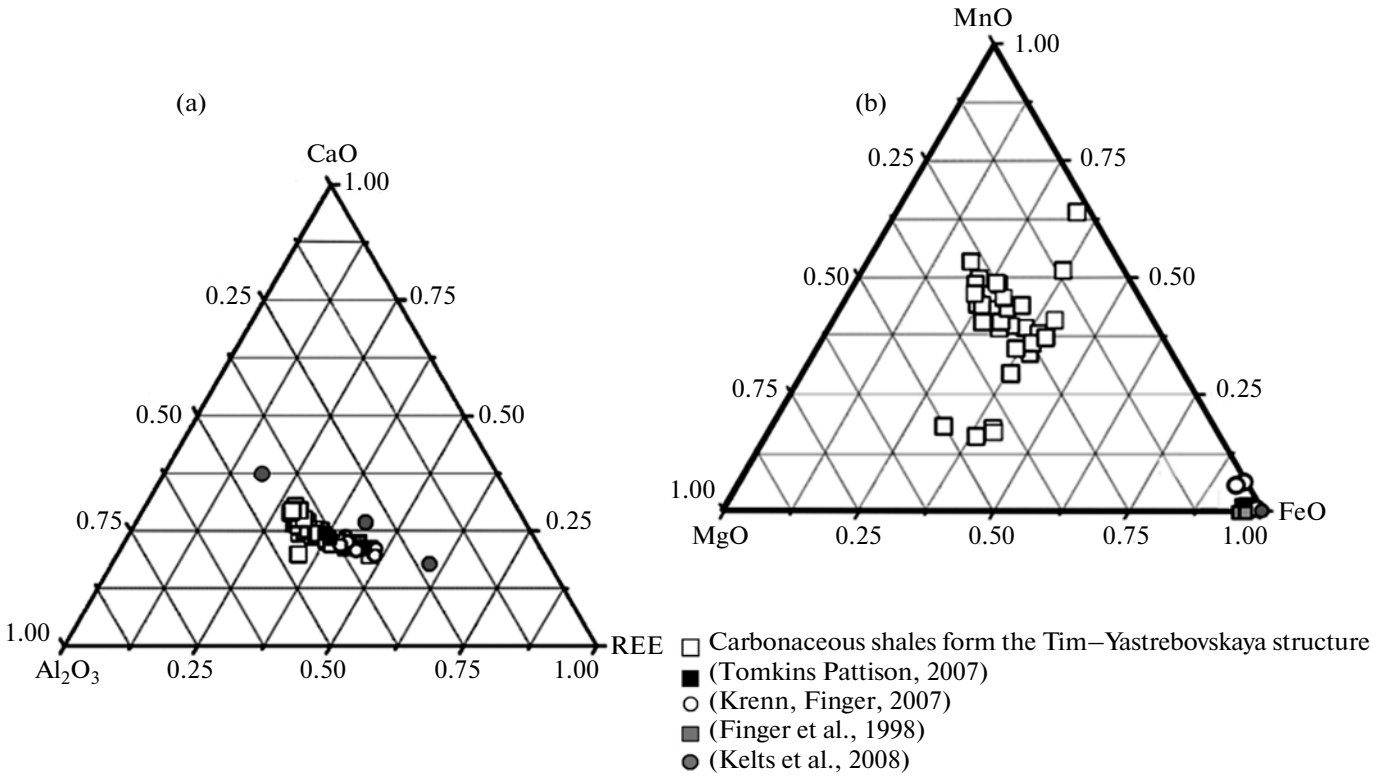

Fig. 9. Allanite composition in diagrams (a) Al_2O_3–CaO–REE and (b) MgO–MnO–FeO.

tals (Fig. 11a). Monazite occasionally replaced apatite in grain rims (Fig. 11b). Monazite (2) is contained in chlorite clusters as anhedral grains up to 50 μm, in close association with sulfides, bastnaesite, allanite, and apatite (Figs. 12b, 12c, 12e). The mineral can also be contained as inclusions in pyrite (Fig. 12a), sometimes together with apatite (Fig. 12d).

When occurring in association with allanite in chlorite clusters, monazite usually forms small resorbed anhedral crystals (Figs. 8a, 8c, 8e, 8f). Occasionally aggregates of very small xenotime and monazite grains were found (Fig. 12f).

The two types of monazite show no differences between their chemical composition (Table 7). All varieties are rich in Ce and contain minor Ca concentrations. The highest concentrations of LREE other than Ce_2O_3 (28.7–33.3 wt %) are those of La_2O_3 (14.6–18.3 wt %), Nd_2O_3 (8.8–12.4 wt %), Pr_2O_3 (1.46–4.47 wt %), and Sm_2O_3 (0.06–4.26 wt %) (Table 7, Fig. 13). The mineral usually contains minor concentrations of Si, which may partly substitute P. The monazite is generally characterized by high concentrations of the Ce-group REE (66–72% respective oxides).

The fact that the monazite contains Pb (up to 1 wt % PbO) is accounted for by the generation of this element by the radioactive decay of U and Th. Considering the Paleoproterozoic age of the carbonaceous shales, radiogenic Pb can be readily accumulated in concentrations sufficient for microprobe analysis, and this provides a basis for the chemical dating of monazite on CHIME (Suzuki et al., 1994).

Bastnaesite is an REE fluorcarbonate of the parisite group, having the empirical formula [(Ce, La)(CO_3)F]. It is the predominant REE mineral in the chlorite clusters. Bastnaesite occurs in the matrix as long (up to 200 μm) elongated prismatic crystals (Fig. 14a). The chlorite clusters sometimes contain small rosettes of acicular crystals 10–20 μm long (Figs. 14b, 14d, 14e) and rims around chlorite (Figs. 14c, 10a, 10b) and tiny inclusions in it (Figs. 8b, 14b–14d). Bastnaesite occurs in chlorite clusters in close association with monazite, allanite, and pyrite.

The composition of the bastnaesite is characterized by the predominance of Ce (24.9–37.6 wt % Ce_2O_3) over other REE (Table 8), with the Ce concentration being twice as high as that of La (13.9–19.55 wt % La_2O_3). Other REE contained in appreciable concentrations are Nd (7.9–15.8 wt % Nd_2O_3) and Pr (1.05–4.38 wt % Pr_2O_3). The Th concentrations of the bastnaesite never exceed 3.15 wt % Th_2O_3, and the mineral sometimes does not contain Th at all. The Ca concentration broadly varies: from 2 to almost 9 wt % CaO. The allanite and bastnaesite show similar REE patterns.

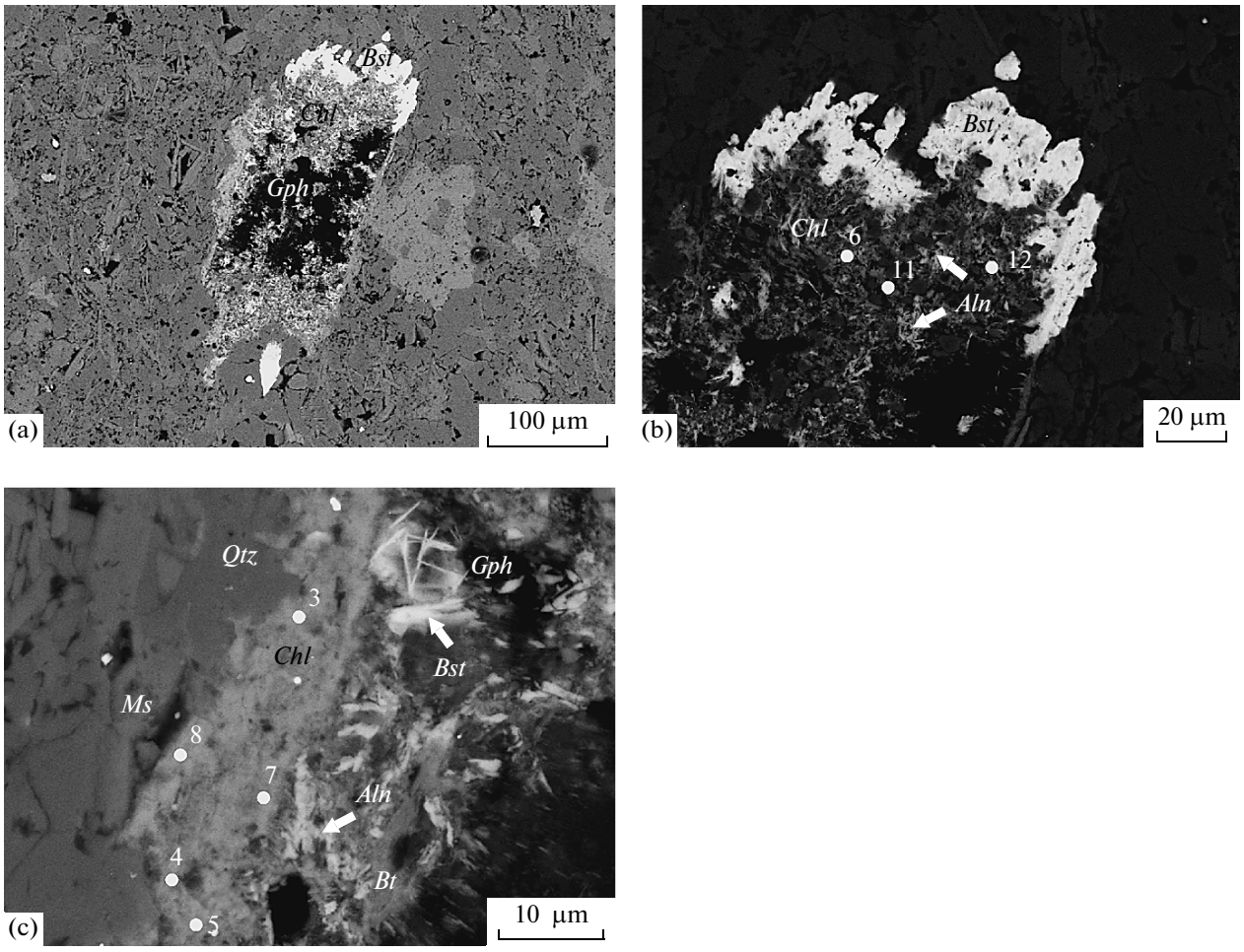

Fig. 10. REE-bearing chlorite in carbonaceous shale from the Tim–Yastrebovskaya structure (analytical spots of microprobe analyses correspond to analysis numbers in Table 6).

(a) Large chlorite grain in the matrix with an inclusion of carbonaceous matter and bastnaesite rims around it (sample 3584/518); (b, c) fragments of this chlorite grain at a higher magnification: chlorite contains allanite and bastnaesite ingrowths.

Bastnaesite often occurs together with synchysite [$Ca(Ce,La,Nd)(CO_3)_2F$], the calcic end member of the bastnaesite–synchysite isomorphic series (Table 8). The mineral occurs in the form of small (no larger than 20 μm; Figs. 8b, 14b) grains. Synchysite differs from bastnaesite in bearing higher concentrations of Ca (15–16 wt % CaO) and, correspondingly, lower concentrations of Ce (25–26 wt % Ce_2O_3) and La (12.7–15.9 wt % La_2O_3) (Table 8).

Similar to monazite and allanite, **apatite** is contained in the carbonaceous shales in two morphological types. Apatite (1) is large grains of equant rounded or irregular morphology, 100–350 μm across, occurring in association with pyrite and rutile. The mineral often contains inclusions of monazite, xenotime, and a phase having a composition (Th,REE) $(Si, P)O_4$ (Figs. 11a, 11d, 11f), although occasional apatite grains are homogeneous and bear no inclusions. Apatite (2) is contained in chlorite clusters in the form of anhedral grains up to 50 μm across, in close association with sulfides, bastnaesite, allanite, and monazite (Figs. 7c, 8a, 8c, 8e, 8f, 11c, 11e, 11f). All of the apatite varieties are F-apatite.

No appreciable REE concentrations were detected in the apatite with monazite inclusions (Table 9). Some grains of matrix apatite without inclusions contain LREE, Th, and U (Table 9).

Phase $(Th,REE)(Si,P)O_4$ (Ce–P huttonite) was detected in the form of inclusions in apatite, together with monazite, as small anhedral inclusions no larger than 30 μm (Fig. 11f). The predominant element of the phase is Th (38–45.6 wt % ThO_2), with its concentrations being twice as high as those of Si (15.3–22.3 wt % SiO_2) (Table 10). The mineral contains minor amounts of P (up to 5 wt % P_2O_5), Ca (up to 1.7 wt % CaO), Fe (up to 1.3 wt % FeO), Pb (up to

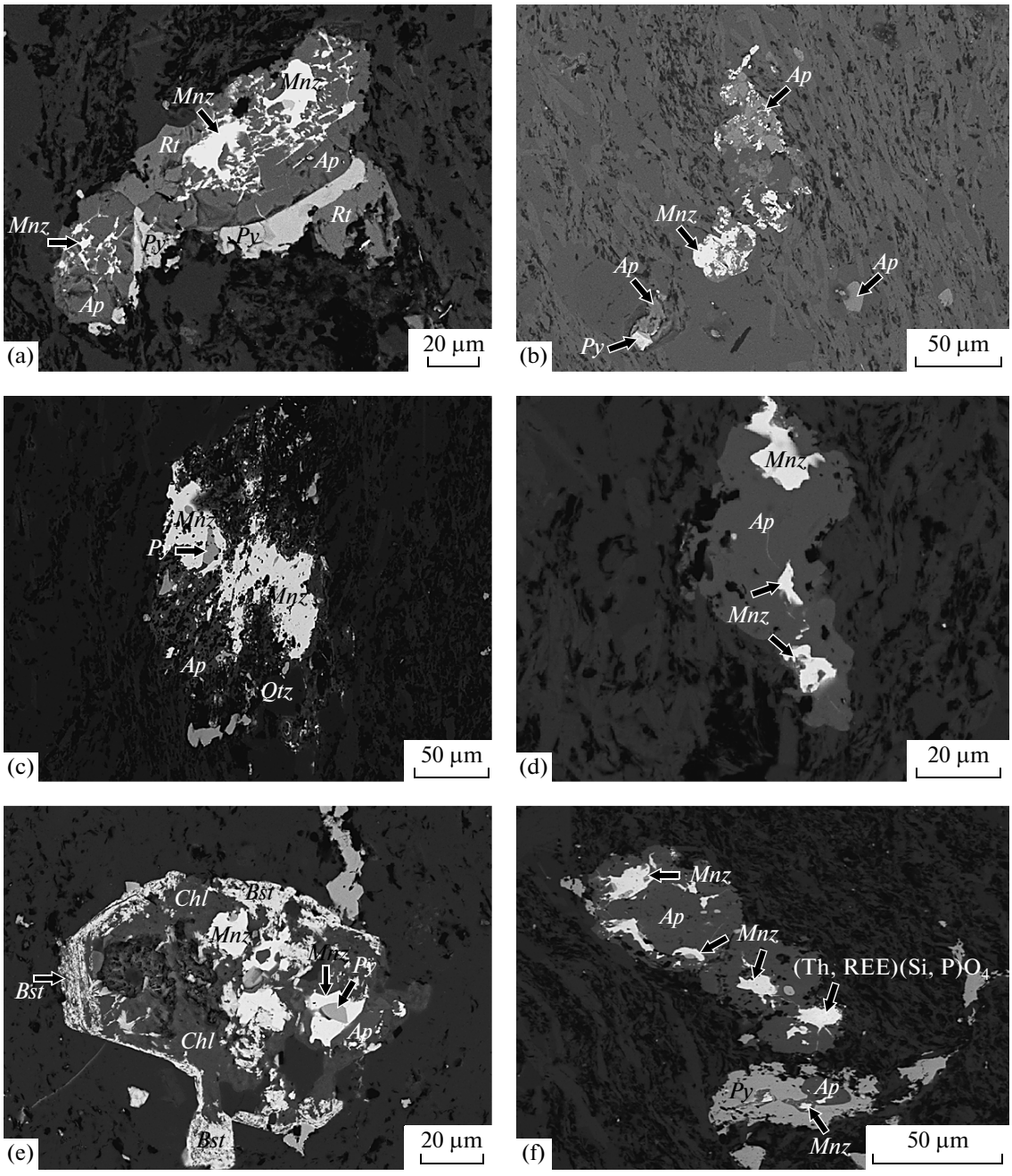

Fig. 11. Relations of apatite and monazite in carbonaceous shales from the Tim–Yastrebovskaya structure.
(a) Numerous monazite inclusions in apatite (sample 3527/496); (b) apatite replaced by monazite in the matrix (sample 3527/508); (c) apatite and monazite in the matrix, monazite contains pyrite inclusions (sample 3527/508); (d) amoeba-shaped monazite inclusions in apatite (sample 3527/508); (e) monazite, apatite, and bastnaesite in a chlorite cluster (sample 3523/573); (f) inclusions of monazite and a phase of the composition (Th,REE)(Si,P)O_4 in apatite (sample 3527/496).

2 wt % PbO), and U. The contents of REE oxides exceed 11 wt %, with the predominance of HREE (Fig. 13). The presence of P and REE is explained by the continuous isomorphic series between huttonite and monazite and, consequently, coupled substitutions $Th^{+4}Si^{+4} \longleftrightarrow Ce^{+3}P^{+5}$.

Zircon–Thorite Solid Solutions

We found minerals of composition intermediate between zircon and thorite in a sample of the carbonaceous shale (sample 3053/220). One of the minerals was detected as a grain 20 × 30 μm whose core consists of thorite and the broad outer zone is

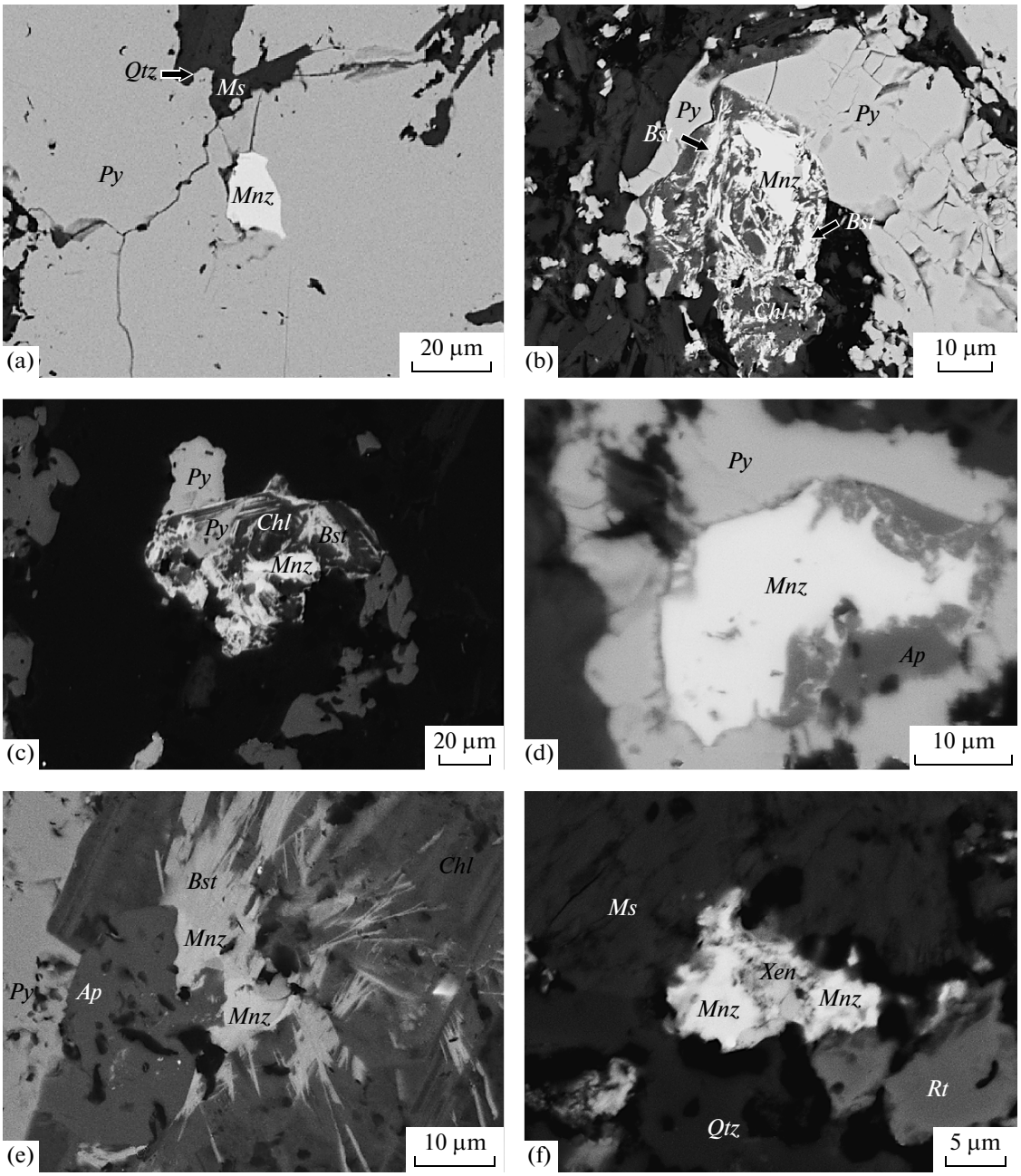

Fig. 12. Relations of monazite in carbonaceous shales from the Tim–Yastrebovskaya structure.
(a) Monazite inclusion in pyrite (sample 3527/508); (b) monazite in chlorite in association with bastnaesite (sample 3527/496); (c) monazite and bastnaesite in a chlorite cluster (sample 3523/510.5; (d) reaction relations of apatite and monazite (sample 3527/508); (e) small monazite and bastnaesite grains at a contact between apatite and chlorite (sample 3620/299.5); (f) aggregate of monazite and xenotime (sample 3527/496).

Zr-bearing thorite (Fig. 15a) with 8.22–10.36 wt % ZrO_2 (Table 10). Thorite differs from Zr-thorite in having higher concentrations of Y_2O_3, Ce_2O_3, and Nd_2O_3 (2.72–3.50, 3.27–3.54, and 3.15–3.40 wt %, respectively).

The other mineral is unzoned Th-bearing zircon, whose grains reach 20–25 μm across (Fig. 15b) and contain 27.2–27.7 wt % ZrO_2 and 23.2–24.9 wt % ThO_2. Other components contained in concentrations of no lower than 1–2 wt % are UO_3, Y_2O_3, Ce_2O_3, Nd_2O_3, PbO, and CaO (Table 10). The elevated (REE + Y) concentrations are caused by the heterovalent substitution $2(REE + Y)^{3+}(Ca + Fe)^{2+} \longleftrightarrow 2(Th,$

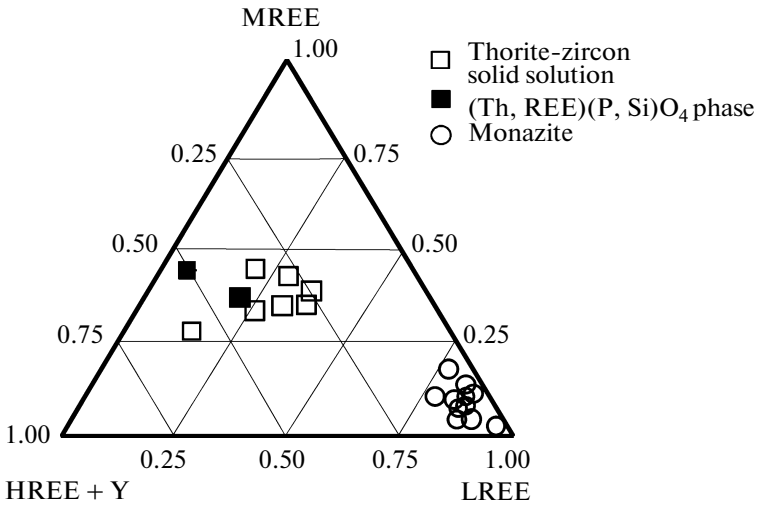

Fig. 13. Composition of monazite, Ce–P huttonite, and thorite-zircon solid solution in carbonaceous shales from the Tim–Yastrebovskaya structure.

Zr, U)$^{4+}$. Th-zircon contains inclusions of Pb sulfoselenide (Fig. 15b, analytical spots *3* and *5*; Table 10).

The low analytical total of microprobe analyses of the thorite, zircon, and Ce–P huttonite (Table 10) are explained, first of all, by the presence of adsorbed water, whose concentrations in thorite may be as high as 15–17 wt % (Speer, 1982; Farges and Callas, 1991).

INTERPRETATIONS OF MINERAL EQUILIBRIA

Genesis of Allanite

As was mentioned above, allanite occurs in the highly carbonaceous metapelites of the Timskaya Formation in two types of mineral assemblages: (1) in close association with chlorite, pyrite, and bastnaesite, in which it can form rims around pyrite and contain bastnaesite inclusions in the matrix (Figs. 7a, 7f), and in chlorite clusters (Fig. 8b); and (2) allanite coexisting with apatite and monazite in the presence of pyrite and, sometimes, bastnaesite (Figs. 8a, 8c, 8e, 8f), with the monazite showing evidence of resorption.

In the second type of assemblages, allanite was formed by a reaction of the partial decomposition of monazite. A number of such reactions were suggested in recently published paper (Wing et al., 2003; Janots et al., 2008) (Table 11). All of these reactions involve Ca- and Fe-bearing silicates or carbonates, together with monazite, in their left-hand parts and apatite in the right-hand ones, as is necessary for mass balance. With regard for the fact that pyrite is widespread in the mineral assemblages in question, allanite could be produced in them by similar reactions but involving pyrite and Mn-bearing silicates (spessartine) or carbonates (Mn-calcite)

$$\begin{aligned} &Mnz + Py + \mathrm{Ca}^{2+} \\ &+ \mathrm{Mn}^{2+}(\text{in silicate and/or carbonate}) \\ &\longrightarrow Aln + Ap + \text{fluid } (\mathrm{H_2O}, \mathrm{CO_2}, \mathrm{S_2}). \end{aligned} \quad (1)$$

Note that the REE patterns of the monazite, allanite, and bastnaesite are almost identical and show strong LREE predominance.

We did not found detrital mineralize in carbonaceous shale of the Timskaya Formation, because this mineral has probably not survived the greenschist-facies metamorphism. In the absence of monazite, LREE could have been borrowed from bastnaesite (synchysite) and LREE-bearing chlorite. Bastnaesite is widespread in the chlorite clusters, although its single large crystals also occur in the groundmass of the rock. Small bastnaesite crystals are restricted to chlorite and form acicular and rosette-shaped aggregates and rims replacing chlorite. These textures are explained by bastnaesite crystallization during the partial replacement of LREE-bearing (up to 2.5 wt %) chlorite. This mechanism was earlier suggested in (Lanzirotti and Hanson, 1996), in which LREE concentrations in chlorite were determined to be of the order of 1000 ppm. Further support to this hypothesis comes from the LREE distribution patterns of chlorite, which the lowest concentrations of these elements detected in zones adjacent to allanite ingrowths and bastnaesite rims. The richness of the metamorphic fluid in F is corroborated by fluid inclusions in calcite occurring in contact with chlorite that is rimmed by bastnaesite

$$Chl_{\mathrm{REE}} + Cal + Flu \longrightarrow Chl + Bst + \mathrm{H_2O}. \quad (2)$$

Allanite ingrowths in REE-bearing chlorite, reaction textures of bastnaesite replacement by allanite, and REE distribution in the chlorite led us to suggest

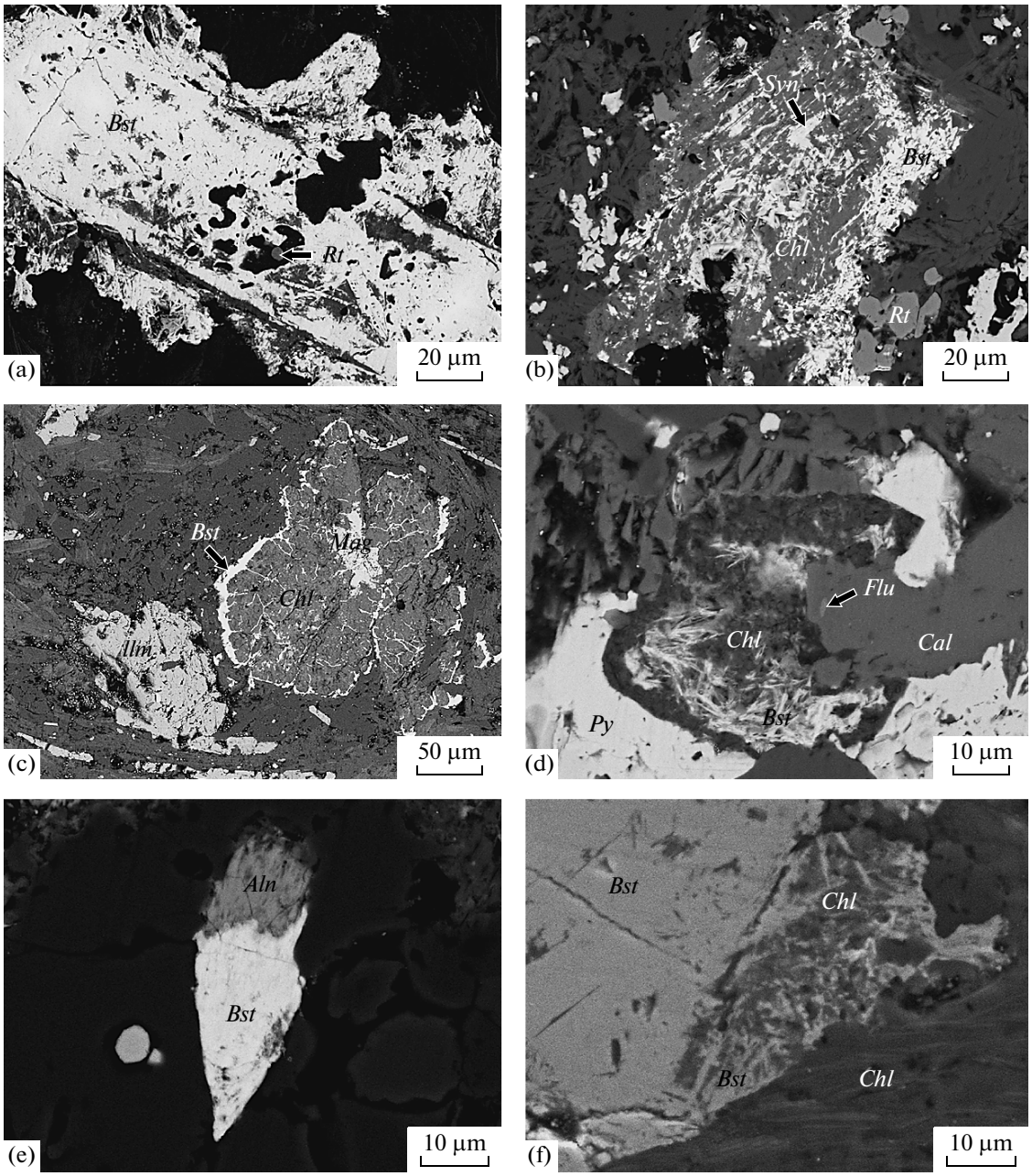

Fig. 14. Bastnaesite in carbonaceous shales from the Tim–Yastrebovskaya structure.
(a) Large prismatic crystal in the matrix (sample 3063/330); (b) bastnaesite and synchysite in chlorite (sample 3527/496); (c) bastnaesite rims around chlorite (sample 3063/329); (d) chlorite replacement by bastnaesite in the presence of calcite with fluorite inclusions (sample 3524/518); (e) bastnaesite replacement by allanite (sample 3524/518); (f) chlorite replacement by bastnaesite (sample 3063/496).

that the allanite was formed by the partial decomposition of REE-bearing chlorite in the presence of calcite

$$Chl_{REE} + Cal \longrightarrow Chl + Aln + CO_2 \quad (3)$$

or a reaction of bastnaesite (synchysite) and chlorite, particularly considering the fact that the bastnaesite contains 2–9 wt % CaO

$$Bst(Ca) + Chl \longrightarrow Aln + \text{fluid } (H_2O, CO_2, HF). \quad (4)$$

Monazite Genesis

Reactions forming monazite via the decomposition of allanite at a temperature increase in the vicinity of the staurolite isograde involve allanite and apatite in their left-hand parts and monazite and a Ca-, Al-, and Fe–Mg-bearing phase in the right-hand parts (Table 11). We have not found any textures of the reaction replacement of allanite by monazite in our metapelites. Although allanite and monazite can

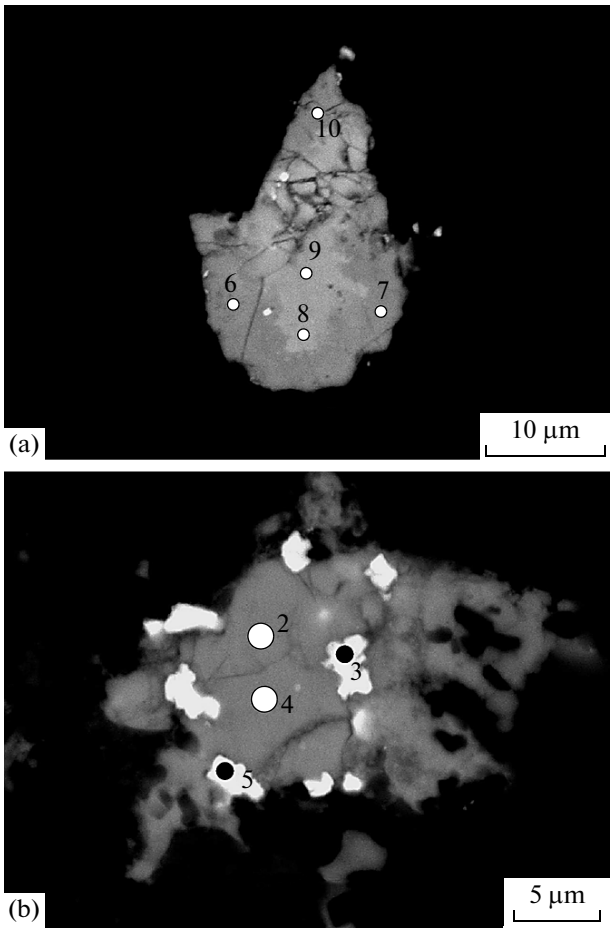

Fig. 15. Zircon-thorite solid solution in carbonaceous shales from the Tim–Yastrebovskaya structure.

(a) Zr-thorite: the grain core (paler) consists of thorite (microprobe analytical spots 8, 9 in Table 10), and the darker broad outer rims consist of thorite (microprobe analytical spots 6, 7, and 10) (sample 3053/220); (b) Th-zircon (microprobe analytical spots 2, 4) with inclusions of Pb sulfoselenite (microprobe analytical spots 3, 5) (sample 3053/220). The numbers of analytical spots correspond to analysis numbers in Table 10.

occur in the same association in some chlorite clusters, they show no reaction relations. Monazite without allanite is often contained in chlorite clusters in close association with bastnaesite, in which the former mineral is newly formed (Figs. 7c, 11e, 12b, 12c, 12e). This provided us with a good ground to think that the monazite was formed by the reaction

$$Bst + Ap \longrightarrow Mnz + Cal + \text{fluid (HF, } H_2O). \quad (5)$$

Another very widely spread type of reaction textures is the replacement of apatite by monazite (Figs. 11b, 11c, 11e, 12f), with no other REE detected in the minerals (Figs. 11a, 11d, 11f). This led us to believe that the monazite crystallized immediately from REE-enriched apatite according to the reaction

$$Ap_{\text{LREE}} \longrightarrow Ap + Mnz + \text{fluid (HF, } H_2O). \quad (6)$$

This is corroborated by the absence of REE from the apatite replaced by or containing inclusions of monazite.

DISCUSSION

Crystallization Succession of LREE-Bearing Phases during Metamorphism

The general crystallization succession of LREE-bearing index minerals during prograde metamorphism in metapelites is as follows: detrital monazite ⟶ metamorphic allanite ⟶ metamorphic monazite (Smith and Barero; Wing et al., 2003; Janots et al., 2009; and others); metamorphic monazite is thought to be replaced by apatite at high temperatures (Finger and Krenn, 2007). The temperature of these replacement reactions, their mechanisms, and the possibility that not only detrital (or magmatic) but also metamorphic monazite can exist at low temperature is a matter of heated debates. Instances when monazite and allanite occur in the same mineral assemblage are fairly rare, with either allanite or monazite growing in the course of prograde metamorphism due to the effect of Ca and Al concentrations in the rocks on the stability of allanite.

Monazite is thought to be a metastable (detrital or magmatic) phase at very low-temperature metamorphic, although newly formed grains of this mineral sometimes reportedly grew during diagenesis in the course of pre-greenschist facies metamorphism (Rasmussen et al., 2001; Evans et al., 2002; Wing et al., 2003; and others).

Phase equilibria at the *Mnz* ⟶ *Aln* ⟶ *Mnz* transitions were recently discussed in detail in (Wing et al., 2003; Tomkins and Pattison, 2007; Janots et al., 2009). As was shown in (Wing et al., 2003), allanite can be produced in metapelites via the decomposition of detrital or metamorphic monazite within the greenschist facies at the biotite isograde. The decomposition of allanite with the forming of monazite is correlated with the appearance of andalusite or kyanite, cordierite, and staurolite. It was determined (Tomkins and Pattison, 2007) that the *Aln* ⟶ *Mnz* transition in the Nelson contact aureole occurred at a temperature close to that of the breakdown of the muscovite–chlorite association with the forming of staurolite or the association of cordierite and andalusite.

The conditions under which allanite is synthesized and decomposes are uncertain as of yet, and the factors controlling its stability have not been identified. The stability field of dissakisite, a magnesian variety of allanite, was calculated from thermochemical data and spans a temperature range of 250–550°C at a broadly varying pressure (Yanots et al., 2007). Most researchers admit that allanite replaces monazite at 400–450°C and remains stable up to the amphibolite facies (Smith and Barero, 1990; Wing et al., 2003; and others). Monazite appears again in the temperature

Table 2. Chemical composition (wt %) of carbon-bearing rocks of the Lower Timskaya Subformation

Component	Quartz–muscovite and muscovite–quartz carbonaceous shales												
	3066/279*	3066/280	3066/281	3066/215	3054/360	3526/222	3526/298	3063/300	3063/579	3063/627	3523/380	3523/418	3523/418
SiO_2	57.50	57.60	58.20	51.80	65.22	56.80	49.66	62.69	55.86	51.66	54.60	61.31	51.16
TiO_2	0.56	0.57	0.53	0.55	0.52	0.43	0.48	0.61	0.87	0.92	0.38	0.45	0.45
Al_2O_3	9.90	13.23	9.10	10.30	13.37	11.92	11.23	11.64	13.57	15.61	16.00	11.03	14.55
Fe_2O_3	1.83	4.18	2.24	4.93	0.87	2.73	3.05	2.39	1.85	1.86	0.12	0.95	1.23
FeO	3.20		3.27	3.98	4.17	1.86	0.79	1.81	7.39	7.66	4.09	2.83	4.91
MnO	0.08	0.05	0.07	0.07	0.07	0.05	0.26	0.11	0.14	0.10	0.06	0.05	0.12
MgO	1.44	1.31	0.1	0.1	1.04	2.01	0.87	3.34	2.30	1.50	1.17	1.21	1.22
CaO	1.33	0.75	2.21	2.21	0.73	0.93	3.87	2.72	2.16	2.56	0.93	0.98	1.94
Na_2O	0.25	0.14	0.30	0.20	0.23	0.15	0.34	0.94	1.80	1.06	0.54	0.30	1.16
K_2O	3.50	3.15	4.24	3.57	3.40	3.08	2.88	1.87	3.22	5.07	3.78	3.40	2.40
P_2O_5	0.3	0.17	0.23	0.25	0.09	0.12	0.02	0.14	0.38	0.56	0.06	0.06	0.08
CO_2	0.2	–	1.10	1.32	0.16	tr	2.14	–	–	0.30	0.50	–	0.27
C_{org}	17.7	17.0	15.56	16.0	6.5	15.2	18.0	9.0	6.0	6.2	16.0	15.0	16.8
S_{tot}	1.28	2.41	1.19	2.46	1.90	2.33	2.35	1.48	4.42	4.38	1.55	1.57	2.34
Component	Quartz–biotite carbonaceous shales												
	3052/229	3052/230	3052/232	3052/233	3063/224	3053/217	3523/303	3039/255	3613/373	3066/220	3066/240	3066/243	3066/275
SiO_2	49.50	56.10	62.70	63.60	55.80	58.30	53.88	54.58	46.69	47.70	47.50	45.70	55.20
TiO_2	0.45	0.42	0.5	0.55	0.61	0.82	0.48	0.51	0.69	0.53	0.62	0.50	0.60
Al_2O_3	5.50	5.60	5.80	7.40	13.30	9.80	14.87	11.96	11.88	9.10	9.60	8.00	11.30
Fe_2O_3	13.46	7.24	5.31	4.11	1.94	2.13	2.35	1.80	1.54	10.71	7.67	12.45	3.26
FeO	5.76	5.84	6.33	6.97	5.55	7.33	2.36	4.59	11.03	3.13	2.84	2.63	5.69
MnO	0.03	0.04	0.05	0.03	0.37	0.68	0.02	0.04	0.18	0.15	0.16	0.25	0.14
MgO	0.10	0.39	2.05	0.32	5.76	6.16	2.68	5.46	1.94	1.58	2.45	2.24	1.50
CaO	2.10	2.21	1.66	0.99	1.11	0.88	5.82	2.09	2.61	1.10	1.33	1.44	1.22
Na_2O	0.3	0.24	0.27	0.34	0.33	0.18	0.62	0.31	1.44	0.21	0.34	0.19	0.32
K_2O	2.30	2.30	1.75	2.15	4.35	1.80	0.96	2.60	2.58	2.26	2.80	2.26	3.20
P_2O_5	0.68	1.45	0.58	0.26	0.17	0.18	0.10	0.09	0.22	0.31	0.28	0.39	0.20
CO_2	1.10	0.20	0.20	0.44	0.20	0.2	tr	0.11	–	0.88	1.52	0.20	0.20
C_{org}	10.50	14.5	9.9	8.8	8.5	8.6	11.14	15.0	14.0	15.5	15.3	17.5	15.4
S_{tot}	6.16	3.29	2.66	2.25	0.76	0.68	1.81	1.01	5.45	4.33	3.28	4.76	1.77

* Sample number.

Table 3. Concentrations (ppm) of minor and trace elements in highly carbonaceous shales from the Tim–Yastrebovskaya structure, ppt*

Element	573/3523	450/3527	475/3527	496/3527	508/3527	327/3063	330/3063	386/3063
Li	33.4	74.2	32.1	23.9	24.4	44.5	50.9	42.5
Be	1.7	0.52	2.3	1.6	1.6	1.6	6.8	1.7
Sc	11.0	20.5	9.5	13.3	8.7	12.6	3.2	12
V	142	229	222	207	183	175	36.4	265
Cr	145	97.8	141	138	131	187	50.2	175
Co	57.8	153.4	11.6	103	48.4	12.4	8.0	79.4
Ni	145	569	114	241	175	257	69.8	376
Cu	91.4	558	443	486	350	229	121	480
Zn	370	84.8	40.6	84.5	309	300	255	270
Ga	25.8	17.3	21.8	20	17	22.4	36.6	21.3
As	120	9.3	1.2	1.7	0.55	<DL	0.42	127
Se	3.3	48.5	15.3	18.7	18	25.1	3.2	21.4
Rb	116	281	120	97.7	96.9	92.7	104	114
Sr	32.2	4.4	42.7	50.9	31.1	22.5	76.6	36.2
Y	7.1	37.2	13.6	15.4	14.5	11.8	46.3	43.9
Zr	126	72.1	132	113	111	177	684	145
Nb	11.0	1.4	4.7	3.1	3.6	9.6	109	9.4
Mo	1.3	4.0	3.4	14.1	4.3	15.7	1.3	8.5
Ag	0.41	0.73	0.45	0.37	0.21	0.29	<DL	1.7
Cd	2.1	0.12	0.076	0.44	1.2	1.1	<DL	1.4
Sn	6.2	1.7	3.0	2.8	2.3	5.6	7.7	3.5
Sb	0.91	5.4	3.5	4.1	0.92	1.6	2.7	12.3
Te	<DL	3.1	1.7	2.1	1.7	1.9	1.2	2.4
Cs	6.4	35.1	6.2	6.8	4.6	6.2	25	13.5
Ba	1122	208	416	263	223	307	296	127
La	45.9	18.5	54.3	56	33.5	12.1	144	42.3
Ce	99.2	41.9	105	111	65.4	27.9	345	88.6
Pr	10.1	4.2	11.0	12.5	7	3.4	38.6	9.5
Nd	37.3	18.1	40.4	46.7	25.9	13.3	136	36.1
Sm	6.1	3.6	6.9	8	4.6	2.7	20.3	6.5
Eu	0.93	0.53	1.3	1.4	1	0.51	2.7	1.4
Gd	4.8	4.4	5.7	6.6	4.4	2.9	16.8	6.9
Tb	0.56	0.7	0.7	0.79	0.62	0.47	2.4	1.1
Dy	2.2	5.1	3.0	3.4	3	2.8	11.5	7.1
Ho	0.36	1.3	0.52	0.58	0.58	0.56	2	1.5
Er	1	4.3	1.4	1.6	1.7	1.7	5.2	4.5
Tm	0.15	0.68	0.21	0.24	0.25	0.26	0.7	0.67
Yb	1.1	4.9	1.4	1.6	1.7	1.9	4.5	4.6
Lu	0.17	0.79	0.22	0.25	0.25	0.32	0.59	0.7
Hf	3.8	1.7	3.8	3.0	3.2	5.1	22.3	4.2
Ta	0.67	0.18	0.51	0.27	0.32	0.84	13.7	0.95
W	6.3	0.5	2.8	5.7	2.2	4.1	2.8	4.4
Re	<DL	0.035	0.023	0.044	0.021	0.042	<DL	0.046
Pt	0.033	<0.03	0.064	<0.05	0.039	0.4	<DL	<DL
Hg	0.071	0.12	0.03	0.093	0.11	0.046	0.023	0.21
Tl	2.9	4.5	1.8	1.6	1.4	1.3	2.3	2.8
Pb	35.9	88.7	23.4	24.9	16.7	24.7	20.7	80.8
Bi	0.15	1.1	0.45	0.53	0.36	0.72	0.21	1.3
Th	13.1	2.1	20.6	17.1	18.7	9.9	22.4	16.9
U	2.1	1.6	5.9	6.1	4.8	7.3	1	6.1
ΣREE	216.97	146.2	245.65	266.06	164.4	82.62	776.59	211.47
ΣLREE	155.2	64.9	170.3	179.5	105.9	43.4	527.6	140.4
Ce/Ce*	1.08	1.21	0.99	0.98	0.99	1.1	1.1	1.04
Eu/Eu*	0.5	0.4	0.61	0.57	0.67	0.55	0.43	0.63
$(La/Yb)_n$	29.92	2.70	27.93	25.10	14.3	4.57	22.95	6.59
$(Gd/Yb)_n$	3.61	0.74	3.38	3.41	2.14	1.26	0.71	1.24
$(LREE/HREE)_n$	8.39	1.09	7.05	6.61	4.09	1.70	6.23	2.20

Table 4. Chemical composition and crystal chemical coefficients of allanite from carbonaceous shales of the Tim–Yastrebovskaya structure

Component	Sample 3527/496												Sample 3527/472						Sample 3523/512
	Aln 1*		Aln 2			Aln 3		Aln 4		Aln 5			Aln 1 large grain						Aln 1
			rim		rim	rim											rim		
	21**	22	23	24	25	26	27	1	2	22	23	24	8	9	10	11	12	13	8
SiO_2	35.15	34.61	35.38	35.23	34.49	33.60	33.29	33.95	33.35	34.91	35.04	34.44	35.73	34.84	34.65	35.09	35.84	33.58	33.74
Al_2O_3	22.88	22.90	23.01	24.35	24.28	22.90	23.43	23.36	23.51	23.90	23.32	23.92	23.40	22.45	22.32	23.14	22.99	22.57	21.40
FeO	2.81	2.17	1.69	2.37	1.96	1.80	2.01	2.71	3.56	2.06	2.33	2.31	4.21	4.11	3.15	3.13	2.89	4.39	4.57
Y_2O_3	0.75	0.72	–	–	1.16	0.71	1.50	0.80	1.05	0.32	0.66	0.35	–	–	–	–	–	–	–
La_2O_3	4.67	4.86	3.70	4.25	5.63	4.74	5.86	5.22	3.60	4.59	5.90	4.64	6.40	7.38	5.98	5.41	6.33	6.37	4.26
Ce_2O_3	8.38	8.72	8.84	8.80	9.21	9.04	10.80	8.97	8.48	9.70	9.03	8.90	9.97	10.86	11.41	8.46	9.89	10.45	8.89
Pr_2O_3	0.61	0.43	1.47	–	0.36	2.02	0.96	1.20	1.49	0.92	–	0.58	–	–	–	–	–	–	–
Nd_2O_3	3.06	3.84	4.01	3.78	2.52	3.88	2.31	3.32	2.90	3.20	1.84	3.36	3.48	3.69	2.82	2.78	2.29	2.23	2.67
MnO	4.02	3.89	4.71	4.05	4.36	3.92	3.85	4.04	3.87	4.14	3.40	4.20	3.56	3.96	2.98	2.87	3.45	3.97	6.35
MgO	2.57	2.71	2.43	2.77	2.44	2.35	0.16	2.58	2.42	2.71	2.68	2.16	2.80	2.37	2.45	1.99	2.35	2.34	1.41
Na_2O	0.03	–	–	–	–	–	–	–	–	–	0.12	–	–	–	–	–	–	0.03	–
CaO	14.57	14.99	14.04	14.77	13.58	14.21	14.04	13.67	14.66	14.10	14.66	14.61	13.71	12.91	14.26	15.11	14.02	13.03	9.24
TiO_2	–	–	–	–	–	–	–	–	–	–	–	–	0.17	0.20	0.27	0.53	0.12	–	–
PbO	0.49	–	–	0.02	–	0.18	–	0.09	0.21	–	–	–	–	–	–	–	–	–	–
ThO_2	–	–	–	–	–	0.66	–	0.09	0.20	0.04	0.96	–	–	–	–	–	–	–	–
UO_3	–	–	–	–	–	–	–	–	–	–	0.07	–	–	–	–	–	–	–	–
Total	99.99	99.84	99.28	100.39	99.99	100.01	98.21	100.00	99.30	100.59	100.01	99.84	103.32	102.75	100.08	98.26	100.17	98.93	92.53
Si	2.99	2.95	3.04	2.95	2.94	2.92	2.89	2.92	2.85	2.96	2.98	2.92	2.97	2.97	2.98	3.01	3.05	2.93	3.14
Al	2.29	2.3	2.33	2.41	2.44	2.35	2.40	2.37	2.37	2.39	2.34	2.39	2.34	2.30	2.31	2.38	2.35	2.36	2.35
Fe	0.20	0.15	0.12	0.17	0.14	0.13	0.15	0.2	0.25	0.15	0.17	0.16	0.26	0.26	0.20	0.20	0.19	0.29	0.36
Y	0.03	0.03	–	–	0.05	0.03	0.07	0.04	0.05	0.01	0.03	0.02	–	–	–	–	–	–	–
La	0.15	0.15	0.12	0.13	0.18	0.15	0.19	0.17	0.11	0.14	0.19	0.15	0.20	0.23	0.19	0.17	0.20	0.20	0.15
Ce	0.26	0.27	0.28	0.27	0.29	0.29	0.34	0.28	0.27	0.30	0.28	0.28	0.30	0.34	0.36	0.27	0.31	0.33	0.30
Pr	0.02	0.01	0.05	–	0.01	0.06	0.03	0.04	0.05	0.03	–	0.02	–	–	–	–	–	–	–
Nd	0.09	0.12	0.12	0.11	0.08	0.12	0.07	0.10	0.09	0.10	0.06	0.10	0.10	0.11	0.09	0.09	0.07	0.07	0.09
Mn	0.29	0.28	0.34	0.29	0.32	0.29	0.28	0.29	0.28	0.30	0.25	0.30	0.25	0.29	0.22	0.21	0.25	0.29	0.50
Mg	0.33	0.34	0.31	0.35	0.31	0.30	0.28	0.33	0.31	0.34	0.34	0.27	0.35	0.30	0.31	0.25	0.30	0.30	0.20
Ca	1.33	1.37	1.29	1.33	1.24	1.33	1.31	1.26	1.34	1.28	1.34	1.33	1.22	1.18	1.32	1.39	1.28	1.22	0.92
Na	–	–	–	–	–	–	–	–	–	–	0.02	–	–	–	–	–	–	–	–
Ti	–	–	–	–	–	–	–	–	–	–	–	–	0.01	0.01	0.02	0.03	0.01	–	–
Pb	0.01	–	–	–	–	–	–	–	–	–	–	–	–	–	–	–	–	–	–
Th	–	–	–	–	–	0.01	–	–	–	–	0.02	–	–	–	–	–	–	–	–
U	–	–	–	–	–	–	–	–	–	–	–	–	–	–	–	–	–	–	–
ΣREE	0.55	0.58	0.57	0.51	0.61	0.66	0.70	0.63	0.57	0.58	0.56	0.57	0.60	0.68	0.64	0.52	0.58	0.61	0.54

Notes: Crystal chemical coefficients were calculated by normalizing to 8 cations. This table and tables below do not show REE concentrations below the detection limit. Oxides are given in wt %, elements are in ppm.

* Grain number; ** analysis number.

Table 5. Distribution of ions between major sites in the crystal chemical formulas of allanite from carbonaceous shales from the Tim–Yastrebovskaya structure

Sample			A1	A2	M1	M2	M3
			2+	2+	3+	3+	2+
Sample 3537/496	Aln 1*	21**	0.88Ca **0.12Mn**	0.45Ca 0.55REE	1.00Al	Al	0.29Al **0.17Mn** 0.20Fe 0.33Mg
		22	0.95Ca **0.05Mn**	0.42Ca 0.58REE	0.98Al #0.02	Al	0.28Al **0.23Mn** 0.15Fe 0.34Mg
	Aln 2	23	0.86Ca **0.14Mn**	0.43Ca 0.57REE	0.96Al #0.04	Al	0.37Al **0.20Mn** 0.12Fe 0.31Mg
		24	0.84Ca **0.16Mn**	0.49Ca 0.51REE	1.00Al	Al	0.41Al **0.13Mn** 0.17Fe 0.35Mg
		25	0.85Ca **0.15Mn**	0.39Ca 0.61REE	1.00Al	Al	0.44Al **0.17Mn** 0.14Fe 0.31Mg
	Aln 3	26	0.99Ca **0.01Mn**	0.34Ca 0.66(REE + Th)	0.96Al #0.04	Al	0.29Al **0.28Mn** 0.13Fe 0.30Mg
		27	1.00Ca	0.31Ca 0.70REE	1.00Al	Al	0.40Al **0.28Mn** 0.15Fe 0.28Mg
	Aln 4	1	0.89Ca 0.11Mn	0.37Ca 0.63REE	1.00Al	Al	0.29Al **0.18Mn** 0.20Fe 0.33Mg
		2	0.91Ca **0.09Mn**	0.43Ca 0.57REE	1.00Al	Al	0.25Al **0.19Mn** 0.25Fe 0.31 Mg
	Aln 5	22	0.86Ca **0.14Mn**	0.42Ca 0.58REE	1.00Al	Al	0.39Al **0.16Mn** 0.15Fe 0.34Mg
		23	0.92Ca **0.06Mn** 0.02Na	0.42Ca 0.58(REE + Th)	1.00Al	Al	0.34Al **0.19Mn** 0.17Fe 0.34Mg
		24	0.90Ca **0.10Mn**	0.43Ca 0.57REE	1.00Al	Al	0.39Al **0.20Mn** 0.16Fe 0.27Mg
Sample 3527/472	Aln 1	8	0.82Ca **0.18Mn**	0.40Ca 0.60REÅ	1.00Al	Al	0.34Al **0.07Mn** 0.26Fe 0.35 Mg 0.01Ti
		9	0.86Ca **0.14Mn**	0.32Ca 0.68REE	1.00Al	Al	0.30Al **0.15Mn** 0.26Fe 0.30Mg 0.01Ti
		10	0.96Ca **0.04Mn**	0.36Ca 0.64REE	1.00Al	Al	0.31Al **0.18Mn** 0.20Fe 0.31Mg 0.02Ti
		11	0.91Ca **0.09Mn**	0.48Ca 0.52REE	0.98Al #0.02	Al	0.40Al **0.12Mn** 0.20Fe 0.25Mg 0.03Ti
		12	0.86Ca **0.14Mn**	0.42Ca 0.58REE	0.96Al #0.04	Al	0.39Al **0.11Mn** 0.19Fe 0.30Mg 0.01Ti
		13	Ca 0.79 **Mn 0.21**	0.49Ca 0.61REE	0.97Al #0.03	Al	0.33Al **0.08Mn** 0.29Fe 0.30Mg
Sample 3523/512	Aln 1	8	0.46Ca **0.50Mn** 0.04#	0.46Ca 0.54REE	0.91Al #0.09	Al	0.44Al 0.36Fe 0.20Mg

* Grain number; ** analysis number.

Table 6. Chemical composition and crystal chemical coefficients of REE-bearing chlorite from carbonaceous shales of the Tim–Yastrebovskaya structure

Component	Sample 3524/518											
	3*	4	5	6	7	8	9	11	12	15	16	17
SiO_2	40.9	30.36	30.96	30.21	32.1	29.73	29.63	34.24	31.95	34.39	38.95	37.54
Al_2O_3	15.65	20.08	20.13	16.83	19.73	19.7	19.08	18.03	19.83	20.97	22.56	19.54
FeO	25.6	33.23	33.57	31.48	31.47	30.45	29.33	33.22	30.00	21.51	18.44	25.56
MnÎ	0.56	0.7	0.59	0.53	0.57	0.68	0.4	0.315	0.33	0.67	0.43	0.25
MgO	1.02	1.26	1.47	1.31	1.37	1.37	1.18	1.54	1.52	4.18	5.22	1.23
CaO	1.93	2.14	1.99	1.17	2.38	2.5	2.65	1.24	3.14	0.48	0.87	3.06
Na_2O	0.25	0.36	0.4	0.22	0.63	0.62	0.52	–	0.44	0.41	0.28	0.5
K_2O	0.42	0.38	0.39	0.12	0.57	0.3	0.13	–	–	1.29	1.36	0.47
La_2O_3	–	–	–	0.59	–	0.65	–	–	–	–	–	–
Nd_2O_3	–	–	–	0.45	–	0.64	–	–	–	–	–	–
Ce_2O_3	1.58	1.65	0.73	1.11	–	1.38	1.54	0.945	1.65	–	0.44	2.28
ThO_2	–	–	–	0.73	–	–	–	–	–	–	–	–
Total	87.91	90.16	90.23	84.75	88.82	88.02	84.46	89.53	89.22	84.22	88.66	90.43
Si	4.73	3.44	3.47	3.7	3.62	3.45	3.56	3.91	3.64	3.96	4.21	4.19
Al	2.13	2.68	2.66	2.43	2.62	2.69	2.7	2.43	2.66	2.85	2.88	2.57
Fe^{2+}	2.48	3.14	3.15	3.23	2.97	2.95	2.94	3.17	2.86	2.07	1.67	2.38
Mn	0.05	0.07	0.06	0.06	0.05	0.07	0.04	0.03	0.03	0.07	0.04	0.02
Mg	0.18	0.21	0.25	0.24	0.23	0.24	0.21	0.26	0.26	0.72	0.84	0.2
Ca	0.24	0.26	0.24	0.15	0.29	0.31	0.34	0.15	0.38	0.06	0.1	0.37
Na	0.06	0.08	0.09	0.05	0.14	0.14	0.12	–	0.10	0.09	0.06	0.11
K	0.06	0.05	0.06	0.02	0.08	0.04	0.02	–	–	0.19	0.19	0.07
La	–	–	–	0.03	–	0.03	–	–	–	–	–	–
Nd	–	–	–	0.02	–	0.03	–	–	–	–	–	–
Ce	0.07	0.07	0.03	0.05	–	0.06	0.07	0.04	0.07	–	0.02	0.09
Th	–	–	–	0.02	–	–	–	–	–	–	–	–
$Fe^{2+}/(Fe^{2+} + Mg)$	0.93	0.94	0.93	0.93	0.93	0.92	0.93	0.92	0.91	0.74	0.66	0.92

Notes: Crystal chemical coefficients were calculated by normalizing to 10 cations.
* Analysis number.

range of 450–530°C (Smith and Barero, 1990; Wing et al., 2003; Janots et al., 2008; and others). It was recently established that the temperature of allanite decomposition with the forming of monazite can vary depending on the CaO and Al_2O_3 contents of the rocks (Foster and Parrish, 2003; Wing et al., 2003).

It is still uncertain in which minerals REE had been concentrated before the crystallization of metamorphic allanite and monazite. Some researchers believe that rock-forming monazite can participate in reactions generating monazite. The reasons for this are as follows: REE phases are absent from low-grade metamorphic rocks (Kohn and Malloy, 2004), relations between zoning in coexisting garnet and monazite (Foster and Parrish, 2003; Pyle and Spear, 2003), the first crystallization of monazite exactly on the staurolite isograde (Fitzsimons et al., 2005), and LREE and P concentrations as high as a few dozen ppm in garnet, plagioclase, biotite, muscovite, and chlorite (Lanzirotti and Hanson, 1996). At the same time, other researchers believe that LREE concentrations in rock-forming silicates are obviously too low to generate monazite in metapelites (Simpson et al., 2000; Yang and Pattison, 2006; Rasmussen et al., 2006; Tomkins and Pattison, 2007). These authors think that acces-

Table 7. Chemical composition and crystal chemical coefficients of monazite from carbonaceous shales of the Tim–Yastrebovskaya structure

Component	Sample 299.5/3620				Sample 496/3527													
	1*	2	3	4	1			2				3			4	5		6
	7**	21	22	23	12	13	14	17	18	19	20	28	29	30	1	5	6	4
P_2O_5	30.02	29.45	30.15	28.51	28.74	27.54	27.93	28.12	27.70	27.14	27.26	28.56	26.89	25.30	25.78	25.94	27.40	30.12
SiO_2	0.82	0.59	0.69	0.92	0.61	0.57	0.48	0.63	1.10	0.69	1.10	0.69	0.43	0.75	1.08	0.72	0.94	0.86
ThO_2	2.93	–	0.66	–	4.63	2.36	2.39	5.29	5.53	5.80	4.83	0.90	2.75	2.97	1.16	3.91	4.35	–
UO_3	–	–	–	–	–	1.23	–	–	–	–	–	–	–	–	–	0.93	–	–
La_2O_3	15.66	17.31	17.77	17.16	16.08	18.26	16.67	17.60	16.78	15.99	17.19	17.55	17.39	17.12	14.63	15.79	15.59	15.52
Ce_2O_3	30.76	32.46	33.85	33.16	30.09	33.24	32.65	33.13	30.17	28.77	31.80	33.33	33.50	28.99	33.35	30.54	30.38	35.10
Pr_2O_3	2.95	2.81	2.22	3.90	3.13	2.34	4.23	2.91	4.30	2.61	4.41	4.20	4.36	3.04	3.46	3.81	3.20	2.10
Nd_2O_3	12.05	11.66	13.23	13.43	12.15	10.65	12.25	10.66	11.14	10.58	10.09	13.37	11.49	11.29	10.66	10.60	11.01	12.43
Sm_2O_3	1.62	2.18	–	1.06	2.39	2.31	1.03	–	1.98	1.36	–	1.89	–	2.17	1.55	2.46	1.69	1.84
Gd_2O_3	1.24	1.27	–	–	1.26	1.83	–	1.00	1.48	2.24	1.01	1.53	1.19	1.67	0.93	1.85	1.75	1.46
Dy_2O_3	–	–	–	–	0.15		–	0.87	–	–	–	0.77	0.89	0.29	–	–	–	–
Eu_2O_3	–	0.87	–	–	–	1.73	–	–	–	–	–	–	–	–	–	0.87	–	–
CaO	0.76	0.50	0.37	0.43	0.55	0.44	0.52	0.65	0.81	0.9	0.86	0.3	0.61	0.39	2.79	0.87	0.75	2.11
PbO	–	–	–	–	–	–	–	–	–	0.94	0.45	–	–	–	–	0.79	0.59	–
Total	98.81	99.1	98.94	98.57	99.78	98.15	98.15	100.86	100.99	97.02	99.00	103.9	99.5	93.98	95.39	99.08	97.65	101.54
P	0.99	0.98	1	0.95	0.97	0.92	0.93	0.94	0.93	0.95	0.93	0.93	0.92	0.92	0.88	0.9	0.94	0.95
Si	0.03	0.02	0.03	0.04	0.02	0.02	0.02	0.02	0.04	0.03	0.04	0.03	0.02	0.03	0.04	0.03	0.04	0.03
Th	0.03	–	0.01	–	0.04	0.02	0.02	0.05	0.05	0.05	0.04	0.01	0.03	0.03	0.01	0.04	0.04	–
U	–	–	–	–	–	0.01	–	–	–	–	–	–	–	–	–	0.01	–	–
La	0.23	0.25	0.26	0.25	0.24	0.27	0.24	0.26	0.24	0.24	0.25	0.25	0.26	0.27	0.22	0.24	0.23	0.21
Ce	0.44	0.47	0.48	0.48	0.44	0.48	0.51	0.48	0.44	0.43	0.47	0.47	0.5	0.45	0.49	0.46	0.45	0.48
Pr	0.04	0.04	0.03	0.06	0.05	0.03	0.06	0.04	0.06	0.04	0.06	0.06	0.06	0.05	0.05	0.06	0.05	0.03
Nd	0.17	0.16	0.18	0.19	0.17	0.15	0.17	0.15	0.16	0.16	0.14	0.18	0.17	0.17	0.15	0.16	0.16	0.17
Sm	0.02	0.03	–	0.01	0.03	0.03	0.01	–	0.03	0.02	–	0.03	–	0.03	0.02	0.03	0.02	0.02
Gd	0.02	0.02	–	–	0.02	0.02	–	0.01	0.02	0.03	0.01	0.02	0.02	0.02	0.01	0.03	0.02	0.02
Dy	–	–	–	–	–	–	–	0.01	–	–	–	0.01	0.01	–	–	–	–	–
Eu	–	0.01	–	–	–	0.02	–	–	–	–	–	–	–	–	–	0.01	–	–
Ca	0.03	0.02	0.02	0.02	0.02	0.02	0.02	0.03	0.03	0.04	0.04	0.01	0.03	0.02	0.12	0.04	0.03	0.08
Pb	–	–	–	–	–	–	–	–	–	0.01	–	–	–	–	–	0.01	0.01	–
ΣREE	0.92	0.98	0.95	0.99	0.95	1	0.99	0.95	0.95	0.92	0.93	1.02	1.02	0.99	0.94	0.99	0.93	0.93

Table 7. (Contd.)

Component	Sample 496/3527							Sample 511/3523			Sample 573/3523				Sample 508/3527	
	7							1	2	3	1		2	3	2	3
	6	7	8	9	10	11	12	7	10	14	3	4	6	7	9	11
P_2O_5	28.46	27.21	25.82	26.85	26.58	28.04	27.81	28.92	28.70	29.33	32.64	32.67	31.97	33.98	27.80	27.60
SiO_2	0.71	0.54	0.89	0.17	0.83	0.65	1.51	1.98	0.38	1.33	–	–	–	–	0.85	0.84
ThO_2	0.92	3.34	2.88	4.54	3.21	4.54	5.15	0.85	1.59	1.28	1.08	1.96	2.37	1.39	2.36	6.69
UO_3	–	–	–	–	–	0.18	–	–	–	–	–	–	–	–	0.40	0.32
La_2O_3	16.75	14.97	14.85	15.05	16.12	18.43	15.75	17.45	16.86	17.81	17.14	17.06	17.31	15.89	15.98	17.04
Ce_2O_3	30.19	29.40	30.63	29.36	31.31	32.33	30.95	33.88	33.57	36.86	33.81	33.63	33.89	33.98	28.73	30.79
Pr_2O_3	4.07	3.50	3.64	2.33	1.46	2.80	4.47	4.09	2.01	4.21	3.72	2.89	2.44	3.35	3.00	2.43
Nd_2O_3	12.21	10.95	11.55	10.33	9.30	8.89	10.89	11.87	10.88	11.64	10.51	11.58	11.26	10.98	11.04	9.51
Sm_2O_3	4.26	1.75	3.08	1.78	0.76	1.90	2.36	1.04	1.33	1.13	–	–	–	1.65	2.65	0.06
Gd_2O_3	2.43	1.44	2.14	1.86	0.20	1.44	1.80	–	–	–	–	–	–	–	1.27	1.16
Dy_2O_3	0.83	1.44	1.07	0.25	1.04	–	1.51	–	–	–	–	–	–	–	1.47	1.16
Eu_2O_3	0.85	–	1.47	0.60	–	0.83	1.33	0.90	–	0.87	–	–	–	–	0.89	0.99
CaO	–	–	–	–	–	–	–	0.99	0.35	0.28	0.53	0.53	–	–	1.06	0.81
PbO	–	1.01	0.46	0.55	–	–	0.73	–	0.91	0.21	–	–	–	0.53	–	–
Total	101.68	95.55	98.48	93.67	90.81	100.03	104.26	101.97	96.58	104.93	99.43	100.32	99.24	101.75	98.22	99.4
P	0.95	0.97	0.98	0.98	0.96	0.92	0.93	0.93	0.99	0.93	1.06	1.05	1.06	1.08	0.95	0.94
Si	0.03	0.02	0.01	0.04	0.03	0.06	0.08	0.07	0.02	0.05	–	–	–	–	0.03	0.03
Th	0.01	0.03	0.04	0.03	0.04	0.05	0.01	0.01	0.01	0.01	0.01	0.02	0.02	0.01	0.02	0.06
U	–	–	–	–	–	–	–	–	–	–	–	–	–	–	–	–
La	0.24	0.23	0.23	0.24	0.26	0.27	0.23	0.24	0.25	0.25	0.24	0.24	0.25	0.22	0.24	0.25
Ce	0.43	0.45	0.46	0.46	0.5	0.48	0.44	0.47	0.5	0.51	0.47	0.47	0.48	0.47	0.42	0.45
Pr	0.06	0.05	0.05	0.04	0.02	0.04	0.06	0.06	0.03	0.06	0.05	0.04	0.03	0.05	0.04	0.04
Nd	0.17	0.16	0.17	0.16	0.14	0.13	0.15	0.16	0.16	0.16	0.14	0.16	0.16	0.15	0.16	0.14
Sm	0.06	0.03	0.04	0.03	0.01	0.03	0.03	0.01	0.02	0.01	–	–	–	0.02	0.04	–
Gd	0.03	0.02	0.03	0.03	–	0.02	0.02	–	–	–	–	–	–	–	0.02	0.02
Dy	0.01	0.02	0.01	–	0.01	–	0.02	–	–	–	–	–	–	–	0.02	0.02
Eu	0.01	–	0.02	0.01	–	0.01	0.02	–	–	0.01	–	–	–	–	0.01	0.01
Ca	–	–	–	–	–	–	–	0.04	0.02	0.01	0.02	0.02	–	–	0.05	0.03
Pb	–	0.01	0.01	0.01	–	–	0.01	–	0.01	–	–	–	–	0.01	–	–
ΣREE	1.01	0.96	1.01	0.97	0.94	0.98	0.97	0.94	0.96	1	0.9	0.91	0.92	0.91	0.95	0.93

Notes: Crystal chemical coefficients were calculated by normalizing to 2 cations.

* Grain number; ** analysis number.

Table 8. Chemical composition and crystal chemical formulas of bastnaesite and synchysite from carbonaceous shales of the Tim–Yastrebovskaya structure

Component	Sample 496/3527														
	1*		2		3				4		5		6		
	Bst 1**	Syn 2	Bst 13	Bst 14	Bst 17	Bst 18	Bst 19	Bst 20	Bst 7	Bst 8	Syn 12	Bst 13	Bst 14	Bst 15	Bst 16
F	7.70	7.09	6.97	5.42	6.31	7.82	6.49	6.50	7.10	6.08	6.36	7.33	6.49	6.84	5.58
CaO	3.43	16.00	5.20	5.10	5.47	5.35	4.01	5.51	3.76	4.17	14.99	4.06	6.30	8.87	8.02
ThO_2	3.15	1.39	0.68	1.59	1.39	0.46	0.33	2.11	2.95	1.77	1.17	2.84	2.07	2.08	1.56
UO_3	–	–	–	0.83	–	0.99	–	–	–	–	–	–	0.27	0.68	0.42
Y_2O_3	1.41	0.26	0.68	1.00	1.39	0.46	0.33	0.95	0.58	0.84	1.35	0.85	1.09	1.07	0.81
La_2O_3	18.36	14.94	17.98	13.94	16.30	17.21	18.31	19.06	16.72	16.28	12.70	17.09	16.49	14.78	15.59
Ce_2O_3	31.20	26.07	30.86	24.92	31.76	32.42	32.20	33.31	29.80	29.87	25.46	32.16	29.80	29.69	30.35
Pr_2O_3	2.36	0.88	2.39	1.19	3.38	3.60	2.87	3.02	2.39	2.38	2.50	3.87	2.70	3.99	3.10
Nd_2O_3	11.21	7.47	11.56	7.94	11.26	10.92	12.48	11.87	10.22	10.16	9.63	11.84	10.50	10.96	8.65
Total	78.82	74.1	76.32	61.93	77.26	83.29	77.02	82.55	73.52	71.55	74.16	80.04	75.71	78.96	74.08
F	0.70	1.10	0.59	0.35	0.54	0.80	0.56	0.64	0.67	0.47	0.98	0.68	0.54	0.60	0.44
Ca	0.13	0.96	0.19	0.23	0.20	0.19	0.15	0.19	0.15	0.17	0.45	0.15	0.23	0.29	0.28
Th	0.03	0.02	0.01	0.02	0.01	–	–	0.02	0.03	0.02	0.01	0.02	0.02	0.01	0.01
U	–	–	–	0.01	–	0.01	–	–	–	–	–	–	–	–	–
Y	0.03	0.01	0.01	0.02	0.02	0.01	0.01	0.02	0.01	0.02	0.02	0.02	0.02	0.02	0.01
La	0.24	0.31	0.23	0.21	0.20	0.21	0.24	0.22	0.23	0.22	0.13	0.22	0.21	0.17	0.19
Ce	0.41	0.53	0.39	0.38	0.39	0.40	0.41	0.39	0.41	0.41	0.26	0.40	0.37	0.34	0.36
Pr	0.03	0.02	0.03	0.02	0.04	0.04	0.04	0.03	0.03	0.03	0.03	0.05	0.03	0.04	0.04
Nd	0.14	0.15	0.14	0.12	0.13	0.13	0.16	0.13	0.14	0.14	0.10	0.14	0.13	0.12	0.10

Component	Sample 330/3063		Sample 299.5/3620			
	1		1		1	1
	Bst 1	Bst 2	13	16	Bst 14	Syn 8
F	7.41	7.18	6.48	5.30	7.87	4.37
CaO	2.04	2.01	6.74	7.86	2.51	12.57
ThO_2	–	–	2.52	2.09	–	3.21
UO_3	–	–	–	–	–	0.59
Y_2O_3	1.87	2.30	–	–	1.80	–
La_2O_3	19.03	18.55	16.31	13.88	19.55	12.13
Ce_2O_3	37.63	36.68	28.94	26.40	35.97	25.20
Pr_2O_3	3.31	4.38	2.33	2.77	1.05	3.15
Nd_2O_3	15.75	15.48	10.51	10.33	15.25	9.08
Total	87.04	86.58	73.83	68.63	84.00	70.30
F	0.67	0.80	0.52	0.38	0.82	0.63
Ca	0.07	0.07	0.25	0.3	0.09	0.83
Th	–	–	0.02	0.02	–	0.05
U	–	–	–	–	–	0.01
Y	0.03	0.04	–	–	0.03	–
La	0.23	0.22	0.21	0.18	0.24	0.28
Ce	0.45	0.44	0.37	0.34	0.44	0.57
Pr	0.04	0.05	0.03	0.04	0.01	0.07
Nd	0.18	0.18	0.13	0.13	0.18	0.20

Notes: Crystal chemical formulas were calculated by normalizing to 1 cation for bastnaesite and 2 cations for synchysite.

* Grain number; ** analysis number.

Table 9. Chemical composition of apatite from carbonaceous shales of the Tim–Yastrebovskaya structure

Component	Sample 3523/511			Sample 3527/508			Sample 3523/573	Sample 3527/496				
	1*	2	3	1	2	3	1	1	2	3	4	5
	1**	5	18	1	1	1	5	1	8	5	8	10
F	4.76	4.01	4.49	5.38	3.76	3.56	5.06	4.97	3.72	5.14	5.99	4.70
P_2O_5	38.46	39.13	41.57	38.11	43.88	44.81	44.01	43.88	44.64	40.44	41.77	39.37
CaO	53.61	54.03	57.00	55.48	55.32	56.80	51.16	51.05	51.64	56.57	57.04	55.62
SiO_2	0.35	0.59	0.18	–	–	–	–	–	–	–	–	–
FeO	0.39	0.29	1.19	–	–	–	–	–	–	–	–	–
MnO	–	–	–	–	–	–	–	–	–	0.68	–	–
MgO	–	0.11	–	–	–	–	–	–	–	–	–	–
Al_2O_3	–	0.42	0.18	–	–	–	–	–	–	–	–	–
La_2O_3	–	–	–	–	0.34	–	–	–	–	–	–	–
Tb_2O_3	–	–	–	–	0.39	–	–	–	–	–	–	–
Eu_2O_3	–	–	–	–	–	0.80	–	–	–	–	–	–
PbO	–	–	–	0.14	–	–	–	–	–	–	–	–
ThO_2	–	–	–	0.25	–	–	0.46	–	–	–	–	–
UO_2	–	–	–	0.28	–	–	–	–	–	–	–	–
Total	97.95	98.60	105.90	100.00	103.69	105.97	100.00	100.00	100.00	102.90	105.17	100.00

* Grain number; ** analysis number.

sory LREE minerals could exist under low temperatures (and are now decomposed) and ensure the crystallization of monazite and allanite.

The spectrum of REE-bearing minerals contained in metapelites is not very broad: these are monazite, allanite, xenotime, REE-apatite, sphene, zircon, and very rare thorite. The secondary minerals replacing monazite are REE phosphates: rhabdophane $CePO_4 \cdot nH_2O$ and florencite $CeAl_3(PO_4)_2(OH)_6$ (Nagy et al., 2002; Krenn and Finger, 2007). The rocks occasionally contain bastnaesite (Bingen et al., 1996) and synchysite (Janots et al., 2006).

The fact that carbonaceous shales of the Tim–Yastrebovskaya structure contain, along with allanite, monazite, xenotime, and REE-apatite, also bastnaesite, synchysite, REE-bearing chlorite, Ce–P huttonite, Nb-aeschynite, xenotime, and zircon–thorite solid solutions is likely explained by the enrichment of these rocks in REE via their adsorption on organic matter in the course of sedimentation and diagenesis (Yudovich and Ketris, 1988). Organic matter is a key factor controlling the behavior of REE during sedimentation in aquatic environments, as follows from data obtained by a diversity of methods: ultrafiltration, electrochemical measurements in waters saturated in organic matter (Dupré et al., 1999; Dia et al., 2000; Johannesson et al., 2004; and others), and experimental studies and model calculations (Davranche et al., 2008; Tang and Johannesson, 2003; Pourret et al., 2007; and others).

The scheme of metamorphic transformations of REE-bearing minerals in sulfide–carbonaceous shales of the Tim–Yastrebovskaya structure differ from those inferred for other complexes, first of all, in that our rocks contain significant amounts of bastnaesite (synchysite) and REE-bearing chlorite, which were stable at the lowest metamorphic grades and, perhaps, also at diagenesis. These minerals played an important part in metamorphic reactions as a LREE source for allanite and monazite. Unfortunately, the lack of data (a merely sparse network of widely spaced boreholes and a thick sedimentary cover) did not allow us to evaluate the temperatures of the reactions forming allanite and monazite at the bastnaesite break-down. However, mineral assemblages in the metapelites indicate that these reactions proceeded at 350–450°C.

Zircon–Thorite Solid Solutions

Intermediate members of the thorite–zircon solid solution were previously found only in aluminous granites and related metasomatites (Föster, 2006). Nowadays relatively numerous microprobe analyses of thorite are available from the literature, but the compositional variability of this mineral is still known inadequately poorly. The reason for this is the fact that thorite is one of the most complex minerals and can contain more than 40 chemical elements in significant concentrations, some of them having variable valences (Speer, 1982).

The problem of the stability of intermediate phases (Th-bearing zircon and Zr-bearing thorite) is put forth in connection with the broad interval of solid solution between hydrous thorite and zircon found in carbon-

Table 10. Chemical composition and crystal chemical coefficients of thorite–zircon solid solution and Ce–P huttonite

Component	Sample 3053/220							Sample 3527/493	Sample 3524/578
	2*	4	6	7	8	9	10	Hut-4	Hut-1
P_2O_5	0.60	0.12	0.62	1.05	1.86	1.67	0.97	5.45	1.90
SiO_2	20.05	18.72	16.44	18.42	15.84	17.37	17.48	15.13	17.66
ZrO_2	27.70	27.23	9.26	8.22	0.43	1.28	10.36	–	–
ThO_2	24.86	23.22	46.66	51.03	53.36	55.55	45.48	45.58	36.07
SO_3	2.56	2.64	1.05	1.10	1.18	0.34	1.43	1.21	–
UO_3	1.08	1.20	1.12	–	–	0.80	1.77	–	15.15
Y_2O_3	1.26	1.66	1.37	1.23	2.72	3.50	0.91	–	5.20
La_2O_3	–	–	–	–	–	–	–	–	0.57
Ce_2O_3	1.18	0.93	2.56	2.23	3.54	3.27	1.90	0.40	3.06
Pr_2O_3	–	–	–	–	–	–	–	0.33	0.95
Nd_2O_3	1.19	1.18	3.03	2.66	3.15	3.40	2.19	1.40	2.26
Sm_2O_3	–	–	–	–	–	–	–	1.90	2.76
Gd_2O_3	0.64	–	–	0.64	0.09	0.61	0.02	1.65	2.62
Dy_2O_3	0.25	–	0.40	–	–	1.00	0.66	2.56	1.63
Ho_2O_3	–	0.68	0.64	–	0.02	0.55	–	0.04	–
Eu_2O_3	0.43	0.21	0.06	–	0.34	0.15	–	0.27	0.74
Er_2O_3	–	0.53	0.05	0.44	–	–	–	0.39	–
Tb_2O_3	–	–	–	–	–	0.11	0.48	0.30	1.7
Yb_2O_3	–	–	–	–	–	–	–	1.32	–
Lu_2O_3	0.19	–	0.24	–	0.16	–	–	0.43	–
Tm_2O_3	–	–	0.30	0.58	–	–	0.21	0.83	1.56
FeO	–	–	0.37	0.75	0.75	0.51	0.19	1.31	0.75
MgO	–	0.81	0.24	0.12	–	0.27	0.30	–	–
CaO	2.01	1.92	1.20	1.13	0.94	0.82	1.31	1.76	2.49
PbO	2.59	1.02	0.33	1.19	0.42	0.46	1.23	0.69	1.79
Total	86.59	82.07	85.94	90.79	84.80	91.66	86.89	82.95	98.86
P	0.02	–	0.03	0.04	0.09	0.07	0.04	0.24	0.07
Si	0.86	0.83	0.86	0.90	0.87	0.88	0.88	0.79	0.82
Zr	0.58	0.59	0.23	0.20	0.01	0.03	0.25	–	–
Th	0.24	0.23	0.55	0.57	0.67	0.64	0.52	0.54	0.38
S	0.08	0.09	0.04	0.04	0.05	0.01	0.05	0.05	–
U	0.01	0.01	0.01	–	–	0.01	0.02	–	0.15
Y	0.03	0.04	0.04	0.03	0.08	0.09	0.02	–	0.13
La	–	–	–	–	–	–	–	–	0.01
Ce	0.02	0.02	0.05	0.04	0.07	0.06	0.03	0.01	0.05
Pr	–	–	–	–	–	–	–	0.01	0.02
Nd	0.02	0.02	0.06	0.05	0.06	0.06	0.04	0.03	0.04
Sm	–	–	–	–	–	–	–	0.03	0.04
Gd	0.01	–	–	0.01	–	0.01	–	0.03	0.04
Dy	–	–	0.01	–	–	0.02	0.01	0.04	0.02
Ho	–	0.01	–	–	–	0.01	–	–	–
Eu	–	-	–	–	0.01	–	–	–	0.01
Er	–	0.01	–	0.01	–	–	–	0.01	–
Tb	–	–	–	–	–	–	0.01	0.02	0.03
Lu	–	–	–	–	–	–	–	0.01	–
Tm	–	–	–	0.01	–	–	–	0.01	0.02
Fe	–	–	0.02	0.03	0.03	0.02	0.01	0.06	0.03
Mg	–	0.05	0.02	0.01	–	0.02	0.02	–	–
Ca	0.09	0.09	0.07	0.06	0.06	0.04	0.07	0.1	0.12
Pb	0.03	0.01	–	0.02	0.01	0.01	0.02	0.01	0.02

Notes: Crystal chemical formulas were calculated by normalizing to 2 cations.

* Analysis number.

Table 11. Prograde reactions involving REE minerals in metapelites

Reactions forming allanite	Reference
Mnz + *Ms* + *Ank* + *Sd* + *Qtz* + H_2O = ***Aln*** + ***Ap*** + *Bt* + CO_2	(Wing et al., 2003)
Mnz + *Chl* + *Pl* + *Cal* + *Qtz* = ***Aln*** + ***Ap*** + H_2O + CO_2	(Wing et al., 2003)
Mnz + *Chl* + *Cal* ± *Hem* = ***Aln*** + ***Ap*** + *Xen* + *Cld* + fluid	(Janots et al., 2008)
Mnz + *Chl* + *An* ± *Hem* = ***Aln*** + ***Ap*** + *Xen* + *Cld* + fluid	(Janots et al., 2008)
Reactions forming monazite	
Aln + ***Ap*** + *Ms* + *And* + *Qtz* = ***Mnz*** + *Bt* + *Pl* + H_2O	(Wing et al., 2003)
Aln + ***Ap*** + *Ep*+(Na, K) in *Ms* + Al-Fe-Mg phase = ***Mnz*** + *Xen* + *Pl* + *Bt* ± *St*	(Janots et al., 2008)
Aln + ***Ap*** + Al-Fe-Mg phase (1) = ***Mnz*** + *An* + Al-Fe-Mg phase (2)	(Janots et al., 2008)
Aln + ***Ap*** = ***Mnz*** + *Pl* + *Mag*(?)	(Tomkins, Pattison, 2007)

aceous shales of the Tim–Yastrebovskaya structure. The stability of minerals in the system Th–Zr–Y–U was experimentally examined in the 1950s–1960s, and broad miscibility gaps were discovered in the thorite and zircon solid solution (Mumton and Roy, 1961). These experiments were conducted in a simple system with two end members and in the absence of water, which made the experimental conditions significantly different from natural ones.

CONCLUSIONS

Based on equilibria of REE minerals examined in sulfide-bearing carbonaceous shales of the Tim–Yastrebovskaya structure, an evolutionary sequence of index LREE-bearing minerals during prograde metamorphism was established. This sequence differs from the currently most commonly adapted scheme: detrital *Mnz* ⟶ *Aln* ⟶ metamorphic *Mnz*. On the one hand, we have not found any reaction textures with allanite replacement by monazite and, one the other hand, have established that an important role in the assemblages of REE minerals is played by bastnaesite (synchysite) and REE-bearing chlorite, which are stable at low metamorphic grades.

The broad occurrence of bastnaesite and other LREE minerals was predetermined by the relatively high LREE concentrations (up to 777 ppm) in the sulfide carbonaceous shales, with these elements accumulated in the course of sedimentation and diagenesis by means of adsorption on organic matter.

The occurrence of reaction textures involving LREE-bearing chlorite, bastnaesite, and allanite led us to suggest that the sources of LREE for the high-temperature allanite and monazite were LREE-bearing chlorite and bastnaesite. This is corroborated by the REE patterns of the monazite, allanite, and bastnaesite, which are nearly identical and show the strong predominance of LREE.

Changes in the LREE mineralogy in the course of zonal metamorphism at 350–550°C were controlled by the following succession of transitions: (1) *Mnz* ⟶ *Aln*, Chl_{REE} ⟶ *Bst*, Chl_{REE} ⟶ *Aln*, *Bst* ⟶ *Aln* and (2) *Bst* ⟶ *Mnz* and Ap_{LREE} ⟶ *Mnz*, which can be interpreted as prograde metamorphic reactions.

ACKNOWLEDGMENTS

The authors thank B.E. Borutskii (Institute of the Geology of Ore Deposits, Petrography, Mineralogy, and Geochemistry (IGEM), Russian Academy of Sciences, for detailed reviewing the first variant of the manuscript, which allowed the authors to significantly improve it.

This study was financially supported by the Russian Foundation for Basic Research (project nos. 09-05-00821 and 09-05-10040).

REFERENCES

1. T. Ambruster, P. Bonazzi, M. Akasaka, et al., "Recommended Nomenclature of Epidote-Group Minerals," Eur. J. Mineral **18**, 551–567 (2006).
2. G. V. Artemenko, Doctoral Dissertation in Geology and Mineralogy (Inst. Geokhim, Mineral. Rudoobr. NAN Ukrainy, Kiev, 1998) [in Russian].
3. G. V. Artemenko, E. N. Bartnitskii, and V. I. Myasnyankin, "Uranium-Lead Age of the Magmatic Rocks of the Orel-Timskaya Greenstone Structure of VKM," Dokl. Akad. Nauk Ukr. SSR, No. 7, 113–117 (1992).
4. Yu. A. Balashov, *Trace-Element Geochemistry* (Nedra, Moscow, 1970) [in Russian].
5. B. Bingen, D. Demaiffe, and J. Hertogen, "Redistribution of Rare Earth Elements, Thorium, and Uranium Over Accessory Minerals in the Course of Amphibolite to Granulite Facies Metamorphism: The Role of Apatite and Monazite in Orthogneisses from Southwestern Norway," Geochim. Cosmochim. Acta **60** (8), 1341–1354 (1996).
6. M. Davranche, O. Pourret, G. Gruau, et al., "Competitive Binding of REE to Humic Acid and Manganese Oxide: Impact of Reaction Kinetics on Development of

Cerium Anomaly and REE Adsorption," Chem. Geol. **247**, 154–170 (2008).

7. A. Dia, G. Gruau, G. Olivié-Lauquet, et al., "The Distribution of Rare-Earths in Groundwater: Assessing the Role of Source-Rock Composition, Redox Changes and Colloidal Particles," Geochim. Cosmochim. Acta **64**, 4131–4151 (2000).
8. B. Dupré, J. Viers, J.-L. Dandurand, et al., "Major and Trace Elements Associated with Colloids in Organic-Rich River Waters: Ultrafiltration of Natural and Spiked Solutions," Chem. Geol. **160**, 63–80 (1999).
9. J. A. Evans, J. A. Zalasiewicz, I. Fletcher, et al., Dating Diagenetic Monazite in Mudrocks: Constraining the Oil Window? J. Geol. Soc. London **159**, 619–622 (2002).
10. F. Farges and G. Callas, "Structural Analyses of Radiation Damage in Zircon and Thorite: An X-Ray Absorption Spectroscopic Study," Am. Mineral. **76**, 60–73 (1991).
11. F. Finger and E. Krenn, "Three Metamorphic Monazite Generations in a High-Pressure Rocks from Bohemian Massif and the Potentially Important Role of Apatite in Stimulating Polyphase Monazite Growth along a *PT* Loop," Lithos **95**, 103–115 (2006).
12. F. Finger, I. Broska, M. P. Roberts, and A. Schermaier, "Replacement of Primary Monazite by Apatite-Allanite-Epidote Coronas in an Amphibolite Facies Granite Gneiss from the Eastern Alps," Am. Mineral. **83**, 248–258 (1998).
13. I. C. W. Fitzsimons, P. D. Kinny, S. Wetherley, and D. A. Hollingsworth, "Bulk Chemical Control on Metamorphic Monazite Growth in Pelitic Schists and Implications for U-Pb Age Data," J. Metamorph. Geol **23**, 261–277 (2005).
14. H.-J. Förster, "Composition and Origin of Intermediate Solid Solutions in the System Thorite-Xenotime-Zircon-Coffinite," Lithos **88**, 35–55 (2006).
15. G. L. Foster and R. R. Parrish, "Metamorphic Monazite and the Generation of *P-T-t* Paths," in *Geochronology: Linking the Isotopic Record with Petrology and Textures*, Ed. by D. Vance, W. Muller, and I. M. Villa, Geol. Soc. London Spec. Publ., **220**, 25–47 (2003).
16. D. H. Gibson, S. D. Carr, R. L. Brown, and M. A. Hamilton, "Correlations between Chemical and Age Domains in Monazite, and Metamorphic Reactions Involving Major Pelitic Phases: An Integration of ID-TIMS and SHRIMP Geochronology with Y-Th-U X-Ray Mapping," Chem. Geol. **211**, 237–260 (2004).
17. E. Janots, F. Brunet, B. Goffer, C. Poinssot, M. Burchard, and L. Cemic, "Thermochemistry of Monazite-(La) and Dissakisite-(La): Implications for Monazite and Allanite Stability in Metapelites," Contrib. Mineral. Petrol. **154**, 1–14 (2007).
18. E. Janots, F. Negro, F. Brunet, et al., "Evolution of REE Mineralogy in HP-LT Metapelites of the Septide Complex, Rif, Morocco: Monazite Stability and Geochronology," Lithos **87**, 214–234 (2006).
19. E. Janots, M. Engi, A. Berger, et al., "Prograde Metamorphic Sequence of REE Minerals in Pelitic Rocks of the Central Alps: Implications for Allanite-Monazite-Xenotime Phase Relations from 250 to 610°C," J. Metamorph. Geol. **26**, 509–526 (2008).
20. E. Janots, M. Engi, D. Rubatto, et al., "Metamorphic Rates in Collisional Orogeny from *in Situ* Allanite and Monazite Dating," Geology **37** (1), 11–14 (2009).
21. K. H. Johannesson, J. W. Tang, J. M. Daniels, et al., "Rare Earth Elements Concentrations and Speciation in Organic-Rich Blackwaters of the Great Dismal Swamp, Virginia, USA," Chem. Geol. **209**, 271–294 (2004).
22. A. B. Kelts, M. Ren, and E. Y. Anthony, "Monazite Occurrence, Chemistry, and Chronology in the Granitoid Rocks of the Lachlan Fold Belt, Australia: An Electron Microprobe Study," Am. Mineral. **93**, 373–383 (2008).
23. V. M. Kholin, Extended Abstract of Candidate's Dissertation in Geology and Mineralogy (VGU, Voronezh, 2001).
24. M. J. Kohn and M. A. Malloy, "Formation of Monazite via Prograde Metamorphic Reactions among Common Silicates: Implications for Age Determinations," Geochim. Cosmochim. Acta **68** (1), 101–113 (2004).
25. S. P. Korikovskii, *Metamorphic Facies of Metapelites* (Nauka, Moscow, 1979) [in Russian].
26. E. Krenn and F. Finger, "Formation of Monazite and Rhabdophane at the Expense of Allanite during Alpine Low Temperature Retrogression of Metapelitic Basement Rocks from Grete, Greece: Microprobe Data and Geochronological Implications," Lithos **95**, 130–147 (2007).
27. A. Lanzirotti and G. N. Hanson, "Geochronology and Geochemistry of Multiple Generations of Monazite from the Wepawaug Schist, Connecticut, USA: Implications for Monazite Stability in Metamorphic Rocks," Contrib. Mineral. Petrol. **125**, 332–340 (1996).
28. I. I. Likhanov, V. V. Reverdatto, and A. E. Vershinin, "Fe- and Al-Rich Metapelites of the Teiskaya Group, Yenisei Range: Geochemistry, Protoliths, and the Behavior of Their Material during Metamorphism," Geokhimiya, No. 1, 20–41 (2008) [Geochem. Int. **46**, 17–36 (2008)].
29. C. R. M. McFarlane, J. N. Connelly, and W. D. Carlson, "Monazite and Xenotime Petrogenesis in the Contact Aureole of the Makhavinekh Lake Pluton, Northern Labrador," Contrib. Mineral. Petrol. **148**, 524–541 (2005).
30. F. A. Mumpton and R. Roy, "Hydrothermal Stability Studies of the Zircon-Thorite Group," Geochim. Cosmochim. Acta **21**, 217–238 (1961).
31. R. W. Murray, M. R. Ten Brink Buchholtz, D. L. Jones, et al., "Rare Earth Elements as Indicator of Different Marine Depositional Environments in Chert and Shale," Geology **18**, 268–272 (1990).
32. G. Nagy, E. Draganits, A. Demeny, et al., "Genesis and Transformations of Monazite, Florencite and Rhabdophane during Medium Grade Metamorphism: Examples from the Sopron Hills, Eastern Alps," Chem. Geol. **191**, 25–46 (2002).
33. Y. Pan, "Zircon- and Monazite-Forming Reactions at Manitouwadge, Ontario," Can. Mineral. **35**, 105–118 (1997).
34. T. N. Polyakova, K. A. Savko, and V. Yu. Skryabin, "Petrology of Metapelites and Silicate-Carbonate Rocks of the Tim–Yastrebovskaya Structure, Voronezh

Crystalline Massif," Tr. Inst. Geol. Voronezhsk. Gos. Univ. **35**, 2006 [in Russian].

35. T. N. Polyakova, K. A. Savko, and V. Yu. Skryabin, "Evolutions of Early Proterozoic Metamorphism within Tim-Yastrebovskaya Paleorift, Voronezh Crystalline Massif, East-European Platform: Metapelite Systematic, Phase Equilibrium and *P-T* Conditions," in *Metamorphism and Crustal Evolution*, Ed. by H. Thomas (Atlantic Publishers and Distributors, New Delhi, 2005), pp. 26–72.
36. O. Pourret, M. Davranche, G. Gruau, and A. Dia, "Rare Earth Elements Complexation with Humic Acid," Chem. Geol. **243**, 128–141 (2007).
37. J. M. Pyle and F. S. Spear, "Four Generations of Accessory Phase Growth in Low-Pressure Migmatites from SW New Hampshire," Am. Mineral. **88**, 338–351 (2003).
38. B. Rasmussen, I. R. Fletcher, and N. J. McNaughton, "Dating Low Grade Metamorphic Events by SHRIMP U-Pb Analysis of Monazite in Shales," Geology **29**, 963–966 (2001).
39. B. Rasmussen, J. R. Muhling, I. R. Fletcher, and M. T. D. Wingate, "In situ SHRIMP U-Pb Dating of Monazite Integrated with Petrology and Textures: Does Bulk Composition Control Whether Monazite Forms in Low-Ca Pelitic Rocks During Amphibolite Facies Metamorphism?," Geochim. Cosmochim. Acta **70**, 3040–3058 (2006).
40. K. A. Savko and T. N. Polyakova, "Zonal Metamorphism and Petrology of Metapelites in the Tim-Yastrebovskaya Structure, Voronezh Crystalline Massif," Petrologiya **9** (6), 593–611 (2001) [Petrology **9**, 516–533 (2001)].
41. N. P. Shcherbak, G. V. Artemenko, E. N. Bartnitskii, et al., "Age of felsic Metavolcanics of the Aleksandrovsky and Korobkovsky Areas of the Kursk Magnetic Anomaly (KMA)," Dokl. Akad. Nauk Ukr. SSR: Ser. B, No. 6, 120–123 (1992).
42. R. L. Simpson, R. Parrish, M. P. Searle, and D. J. Waters, "Two Episodes of Monazite Crystallization during Metamorphism and Crustal Melting in the Everest Region of the Nepalese Himalaya," Geology **28**, 403–406 (2000).
43. H. A. Smith and B. Barero, "Monazite U-Pb Dating of Staurolite Grade Metamorphism in Pelitic Schists," Contrib. Mineral. Petrol. **105**, 602–615 (1990).
44. F. S. Spear and J. M. Pyle, "Apatite, Monazite, and Xenotime in Metamorphic Rocks," Rev. Mineral **48**, 1–63 (2003).
45. J. A. Speer, "The Actinide Orthosilicates," Rev. Mineral. **5**, 113–135 (1982).
46. K. Suzuki, M. Adachi, and I. Kajizuka, "Electron Microprobe Observations of Pb Diffusion in Metamorphosed Detrital Monazites," Earth Planet. Sci. Lett. **128**, 391–405 (1994).
47. J. Tang and K. H. Johannesson, "Speciation of Rare Earth Elements in Natural Terrestrial Waters: Assessing the Role of Dissolved Organic Matter from the Modeling Approach," Geochim. Cosmochim. Acta **67**, 2321–2339 (2003).
48. H. S. Tomkins and D. R. M. Pattison, "Accessory Phase Petrogenesis in Relation To Major Phase Assemblages in Pelites from the Nelson Contact Aureole, Southern British Columbia," J. Metamorph. Geol **25**, 401–421 (2007).
49. B. A. Wing, J. M. Ferry, and T. M. Harrison, "Prograde Destruction and Formation of Monazite and Allanite During Contact and Regional Metamorphism of Pelites: Petrology and Geochronology," Contrib. Mineral. Petrol. **145**, 228–250 (2003).
50. P. S. Yang and D. Pattison, "Genesis of Monazite and Y Zoning in Garnet from the Black Hills, South Dakota," Lithos **88**, 233–253 (2006).
51. Ya. E. Yudovich and M. P. Ketris, *Geochemistry of Black Shales* (Nauka, Leningrad, 1988) [in Russian].